Commun Nonlinear Sci Numer Simulat 134 (2024) 108025

Contents lists available at ScienceDirect

Communications in Nonlinear Science and Numerical Simulation

journal homepage: www.elsevier.com/locate/cnsns

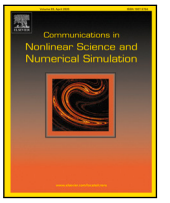

Research paper

The bifurcation structure within robust chaos for two-dimensional piecewise-linear maps

Indranil Ghosh *, Robert I. McLachlan, David J.W. Simpson

School of Mathematical and Computational Sciences, Massey University, Colombo Road, Palmerston North, 4410, New Zealand

ARTICLE INFO

Keywords:
Piecewise-linear maps
Difference equations
Border-collision normal form
Robust chaos
Renormalisation

ABSTRACT

We study two-dimensional, two-piece, piecewise-linear maps having two saddle fixed points. Such maps reduce to a four-parameter family and are well known to have a chaotic attractor throughout open regions of parameter space. The purpose of this paper is to determine where and how this attractor undergoes bifurcations. We explore the bifurcation structure numerically by using Eckstein's greatest common divisor algorithm to estimate from sample orbits the number of connected components in the attractor. Where the map is orientation-preserving the numerical results agree with formal results obtained previously through renormalisation. Where the map is orientation-reversing or non-invertible the same renormalisation scheme appears to generate the bifurcation boundaries, but here we need to account for the possibility of some stable low-period solutions. Also the attractor can be destroyed in novel heteroclinic bifurcations (boundary crises) that do not correspond to simple algebraic constraints on the parameters. Overall the results reveal a broadly similar component-doubling bifurcation structure in the orientation-reversing and non-invertible settings, but with some additional complexities.

1. Introduction

Complex dynamics are caused by nonlinearity, and many physical systems involve an extreme form of nonlinearity: a switch. Examples include engineering systems with relay or on/off control which involve distinct modes of operation [7,23,43]. Mathematical models of systems with switches are naturally piecewise-smooth, where different pieces of the equations correspond to different positions of a switch.

Piecewise-smooth maps arise as discrete-time models of systems with switches [16,33] and as Poincaré maps or stroboscopic maps of continuous-time models [5]. For multi-dimensional piecewise-smooth maps there are many *abstract* ergodic theory results stating that if an attractor satisfies certain properties (e.g. expansion) then it is chaotic in a certain sense (e.g. has an SRB measure) [8,30,35,42,45]. This paper in contrast provides *explicit* results for a physically-motivated family of maps. We study the four-parameter family

$$f_{\xi}(x,y)=\begin{cases}\begin{bmatrix}\tau_L x+y+1\\ -\delta_L x\end{bmatrix}, & x\le 0,\\ \begin{bmatrix}\tau_R x+y+1\\ -\delta_R x\end{bmatrix}, & x\ge 0,\end{cases} \tag{1}$$

* Corresponding author.
E-mail addresses: i.ghosh@massey.ac.nz (I. Ghosh), r.mclachlan@massey.ac.nz (R.I. McLachlan), d.j.w.simpson@massey.ac.nz (D.J.W. Simpson).
URL: http://indrag49.github.io (I. Ghosh).

https://doi.org/10.1016/j.cnsns.2024.108025
Received 6 February 2024; Accepted 11 April 2024
Available online 19 April 2024
1007-5704/© 2024 The Author(s). Published by Elsevier B.V. This is an open access article under the CC BY license (http://creativecommons.org/licenses/by/4.0/).

where $\xi = (\tau_L, \delta_L, \tau_R, \delta_R) \in \mathbb{R}^4$. This is known as the two-dimensional border-collision normal form (BCNF) [26]. This family provides leading-order approximations to border-collision bifurcations where a fixed point of a piecewise-smooth map collides with a switching manifold as parameters are varied [36]. As such (1) can be used to capture the change in dynamics as parameters are varied to pass through border-collision bifurcations. In this regards it has been applied to mechanical oscillators with stick–slip friction [41], DC/DC power converters [47], and various models in economics [33]. We stress that unlike Poincaré maps of smooth invertible flows, the piecewise-smooth maps arising from these applications are mostly non-invertible. We distinguish four generic cases based on the signs of the determinants δ_L and δ_R:

- With $\delta_L > 0$ and $\delta_R > 0$ (1) is orientation-preserving. This is the classical scenario considered in the 'robust chaos' paper of Banerjee et al. [4].
- With $\delta_L < 0$ and $\delta_R < 0$ (1) is orientation-reversing. Misiurewicz [25] used this scenario in the subfamily of Lozi maps ($\tau_L = -\tau_R$, $\delta_L = \delta_R$) for his novel rigorous demonstration of robust chaos.
- With $\delta_L > 0$ and $\delta_R < 0$ (1) is non-invertible mapping both the left half-plane ($x \le 0$) and the right half-plane ($x \ge 0$) onto the upper half-plane ($y \ge 0$). This scenario applies to border-collision bifurcations in a wide range of power converters whereby a switch in a circuit creates non-invertible dynamics [3,6,46].
- With $\delta_L < 0$ and $\delta_R > 0$ (1) is again non-invertible with applications to power electronics, but now maps to the lower half-plane ($y \le 0$) and exhibits different dynamical features (notice (1) maps the origin to the right half-plane so does not have left/right symmetry).

Despite its apparent simplicity (1) has an incredibly complex bifurcation structure that remains to be fully understood [2,10,38,40,47]. The most significant bifurcations are those at which the attractor splits into pieces. In [13] we used renormalisation to uncover an infinite sequence of codimension-one bifurcations. However, this only accommodated the orientating-preserving setting of Banerjee et al. [4]. In this paper we identify similar sequences of bifurcations in the orientation-reversing and non-invertible parameter regimes. Again we use renormalisation to find bifurcations, but now this approach misses some bifurcations. For this reason we combine the analytical framework with brute-force numerical simulations that compute the number of connected components from the behaviour of forward orbits.

The remainder of this paper is organised as follows. We start in Section 2 by reviewing the bifurcation structure of one-dimensional piecewise-linear maps (skew tent maps) and how this structure can be generated through renormalisation. This corresponds to the BCNF in the special case $\delta_L = \delta_R = 0$, and it is helpful to view the bifurcation structures described in later sections as extensions or perturbations from the structure that arises in one dimension. Then in Section 3 we review the parameter region $\Phi \subset \mathbb{R}^4$ where the BCNF has two saddle fixed points. We describe special points on the stable and unstable manifolds of the fixed points whose relation to one another can be used to characterise the occurrence of homoclinic and heteroclinic bifurcations where the attractor is destroyed. In Section 4 we introduce the renormalisation scheme and describe some basic aspects of this scheme that hold for all values of δ_L and δ_R. Then in Section 5 we summarise the results of [13] for the orientation-preserving setting.

Next in Section 6 we describe an algorithm for numerically determining the number of connected components of attractor. The algorithm outputs the greatest common divisor of a set of iteration numbers required for an orbit to return close to its starting point. The algorithm is effective when the components of attractor are not too close to one another and the dynamics on the attractor is ergodic. Applied to the orientation-preserving setting it reproduces the bifurcation structure obtained by renormalisation.

In Sections 7, 8, and 9 we study the orientation-reversing and non-invertible cases and explain why the same renormalisation scheme should be expected to work in these settings. Formal proofs are beyond the scope of this study because, as evident from [13], these require a detailed analysis of the four-dimensional nonlinear renormalisation operator, plus will involve additional complexities because now stable period-two and period-four solutions are possible. Also if $\delta_L < 0$ and $\delta_R > 0$ then the bifurcations that destroy the attractor are different and more difficult to characterise. In Section 10 we describe a special case unique to the non-invertible settings where the dynamics reduces to one dimension. Concluding remarks are provided in Section 11.

2. Skew tent maps

With $\delta_L = \delta_R = 0$ the y-dynamics of (1) is trivial and the x-dynamics reduces to

$$x \mapsto \begin{cases} \tau_L x + 1, & x \le 0, \\ \tau_R x + 1, & x \ge 0. \end{cases} \tag{2}$$

This is a two-parameter family of skew tent maps. For any values of the parameters τ_L and τ_R for which (2) has an attractor, this attractor is unique. Fig. 1 shows typical examples of the attractor using $\tau_L > 1$ and $\tau_R < -1$ with which (2) is piecewise-expanding, so the attractor is chaotic in a strict sense by the results of Lasota and Yorke [21] and Li and Yorke [22]. Fig. 1 shows typical examples of the chaotic attractor. In panel (a) the attractor is the interval $[\tau_R + 1, 1]$ whose endpoints are the first and second iterates of the switching value $x = 0$. In panel (b) the attractor is a disjoint union of four intervals whose endpoints are the first through eighth iterates of $x = 0$.

For all values of τ_L and τ_R the nature of the attractor is well understood [24,27,39]. Fig. 2 shows how the part of the (τ_L, τ_R)-plane that is relevent to us divides into regions according to the number of intervals that comprise the attractor. In the top-left region

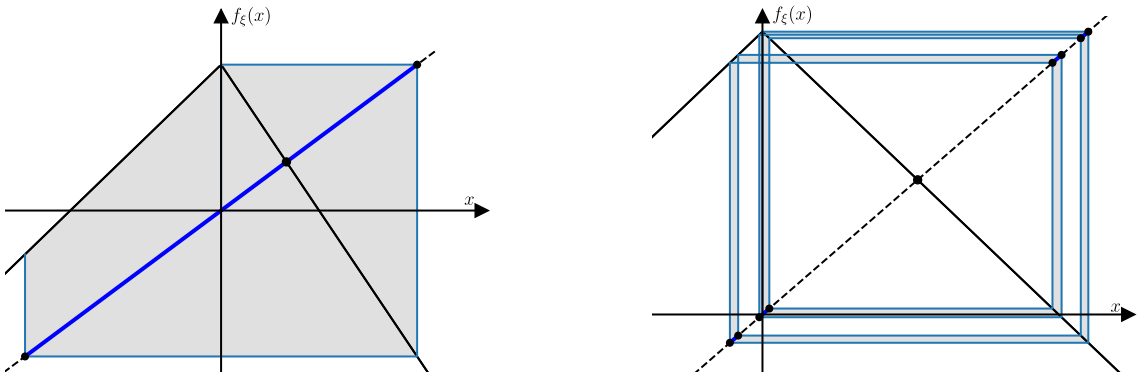

(a) $(\tau_L, \tau_R) = (1.3, -2)$. (b) $(\tau_L, \tau_R) = (1.1, -1.1)$.

Fig. 1. Cobweb diagrams showing the attractor of the skew tent map (2) with two different combinations of the parameter values. In (a) the attractor is an interval; in (b) the attractor is the union of four disjoint intervals. The maps are also instances of the BCNF (1) with $\xi = (1.3, 0, -2, 0)$ in panel (a) and $\xi = (1.1, 0, -1.1, 0)$ in panel (b).

labelled LR the map has a stable period-two solution. This solution has one point in the left half-plane and one point in the right half-plane, so is termed an LR-cycle. This region is bounded by the curve $\alpha_0(\tau_L, \tau_R) = 0$, where

$$\alpha_0(\tau_L, \tau_R) = \tau_L \tau_R + 1, \tag{3}$$

which is where the LR-cycle loses stability by attaining a stability multiplier of -1. The boundary in the lower-right part of the figure is a homoclinic bifurcation where $x = 0$ maps in two iterations to the fixed point of (2) in $x < 0$. This occurs on the curve $\phi_0(\tau_L, \tau_R) = 0$, where

$$\phi_0(\tau_L, \tau_R) = \tau_L \tau_R + \tau_L - \tau_R. \tag{4}$$

As shown by Ito et al. [17,18] the remaining boundaries can be identified through renormalisation as follows. Suppose there exists an interval neighbourhood I of $x = 0$ that maps into $x > 0$, then, on the second iteration, back into I. In this case the restriction of the second iterate of (2) to I is piecewise-linear with two pieces. The $x < 0$ piece corresponds to iterates with symbolic itinerary LR and has slope $\tau_L \tau_R < -1$, while the $x > 0$ piece corresponds to iterates with symbolic itinerary RR and has slope $\tau_R^2 > 1$. Thus the second iterate of (2) on I is conjugate to (2) with τ_R^2 in place of τ_L and $\tau_L \tau_R$ in place of τ_R. This corresponds to the *substitution rule* $(L, R) \mapsto (RR, LR)$, and induces the *renormalisation operator*

$$g(\tau_L, \tau_R) = (\tau_R^2, \tau_L \tau_R). \tag{5}$$

By using the preimages of the homoclinic bifurcation boundary we define the sequence of regions

$$\mathcal{R}_n = \left\{ (\tau_L, \tau_R) \,\middle|\, \tau_R < -1, \phi_0\left(g^n(\xi)\right) > 0, \phi_0\left(g^{n+1}(\xi)\right) \le 0, \alpha_0(\tau_L, \tau_R) < 0 \right\}, \tag{6}$$

shown in Fig. 2. These are non-empty for all $n \ge 0$ and converge to $(\tau_L, \tau_R) = (1, -1)$ as $n \to \infty$. In $\mathcal{R}_0$ the attractor consists of one interval:

Theorem 2.1. *For any $(\tau_L, \tau_R) \in \mathcal{R}_0$ with $\tau_L \ge 1$, the interval $[\tau_R + 1, 1]$ is the unique attractor.*

A simple proof of Theorem 2.1 can be found in Veitch and Glendinning [44]. The condition $\tau_L \ge 1$ is needed because for some $0 < \tau_L < 1$ and $\tau_R < -1$ the attractor is periodic. This condition can be weakened but this is not needed for our purposes.

To characterise the attractor in the other regions $\mathcal{R}_n$ we first make the following observation that follows simply from the definitions of g and $\mathcal{R}_n$.

Proposition 2.2. *If $(\tau_L, \tau_R) \in \mathcal{R}_n$ with $n \ge 1$, then $g(\tau_L, \tau_R) \in \mathcal{R}_{n-1}$.*

Thus if $(\tau_L, \tau_R) \in \mathcal{R}_n$ then $g^n(\tau_L, \tau_R) \in \mathcal{R}_0$. Theorem 2.1 can be applied at this parameter point because any point below $\tau_R = -1$ maps under g to the right of $\tau_L = 1$. Moreover, the above conjugacy can be shown to hold under all n applications of g, see Ito et al. [17,18], thus the 2^n-iterate of (2) has an interval attractor. The images of this interval under (2) give 2^n disjoint intervals and hence the following result.

Theorem 2.3. *If $(\tau_L, \tau_R) \in \mathcal{R}_n$ with $n \ge 1$, then (2) has a unique attractor comprised of 2^n disjoint intervals.*

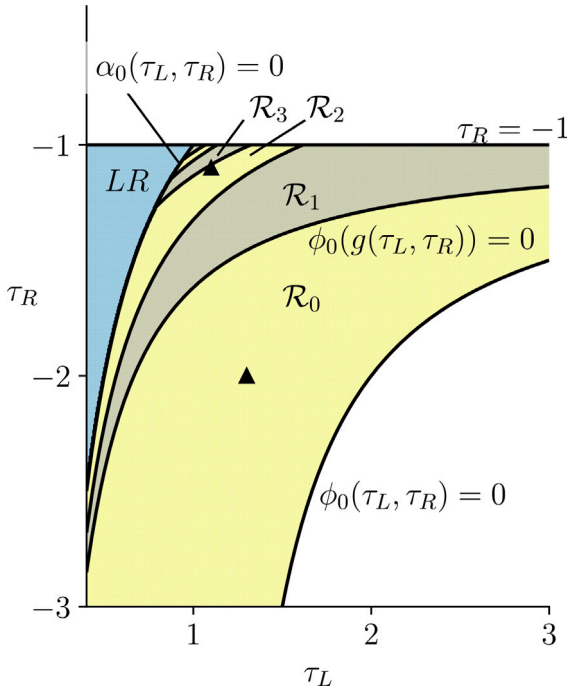

Fig. 2. A two-parameter bifurcation diagram of the skew tent map family (2). In $\mathcal{R}_0$ the attractor is an interval. In each $\mathcal{R}_n$ with $n \geq 1$ the attractor is comprised of 2^n disjoint intervals. Below $\phi_0(\tau_L, \tau_R) = 0$ the map has no attractor; above $\tau_R = -1$ it has a stable fixed point in $x > 0$; in the top-left region it has a stable LR-cycle (period-two solution). The triangles indicate the parameter values used in Fig. 1.

3. Two-dimensional piecewise-linear maps with two saddle fixed points

We now return to the BCNF (1) with non-zero values of δ_L and δ_R. In this section we identify two saddle fixed points and compute some important points on their stable and unstable manifolds.

Motivated by Banerjee et al. [4] we focus on the following subset of four-dimensional parameter space:

$$\Phi = \left\{ \xi \in \mathbb{R}^4 \;\middle|\; \tau_L > |\delta_L + 1|, \tau_R < -|\delta_R + 1| \right\}. \tag{7}$$

It is a simple exercise to show that Φ is the set of all parameter values for which (1) has two saddle fixed points [11]. These fixed points are

$$X = \left(\frac{-1}{\tau_R - \delta_R - 1}, \frac{\delta_R}{\tau_R - \delta_R - 1} \right), \tag{8}$$

$$Y = \left(\frac{-1}{\tau_L - \delta_L - 1}, \frac{\delta_L}{\tau_L - \delta_L - 1} \right), \tag{9}$$

where X is in the open right half-plane $x > 0$, and Y is in the open left half-plane $x < 0$. Let

$$A_L = \begin{bmatrix} \tau_L & 1 \\ -\delta_L & 0 \end{bmatrix}, \qquad A_R = \begin{bmatrix} \tau_R & 1 \\ -\delta_R & 0 \end{bmatrix}, \tag{10}$$

denote the Jacobian matrices associated with Y and X respectively. With $\xi \in \Phi$ the matrix A_L has eigenvalues $|\lambda_L^s| < 1$ and $\lambda_L^u > 1$, while A_R has eigenvalues $|\lambda_R^s| < 1$ and $\lambda_R^u < -1$.

Since X and Y are saddles their stable and unstable manifolds are one-dimensional, and since the map is piecewise-linear these manifolds are piecewise-linear. Their stable manifolds $W^s(X)$ and $W^s(Y)$ have kinks on the switching manifold $x = 0$ and at preimages of these points, while their unstable manifolds $W^u(X)$ and $W^u(Y)$ have kinks on the image of the switching manifold $y = 0$ and at images of these points. For instance, as we grow $W^u(X)$ outwards from X, in one direction its first kink occurs at the point

$$T = \left(\frac{1}{1 - \lambda_R^s}, 0 \right), \tag{11}$$

on $y = 0$, see Fig. 3. Similarly as we grow $W^u(Y)$ outwards from Y, in one direction its first kink occurs at

$$D = \left(\frac{1}{1 - \lambda_L^s}, 0 \right). \tag{12}$$

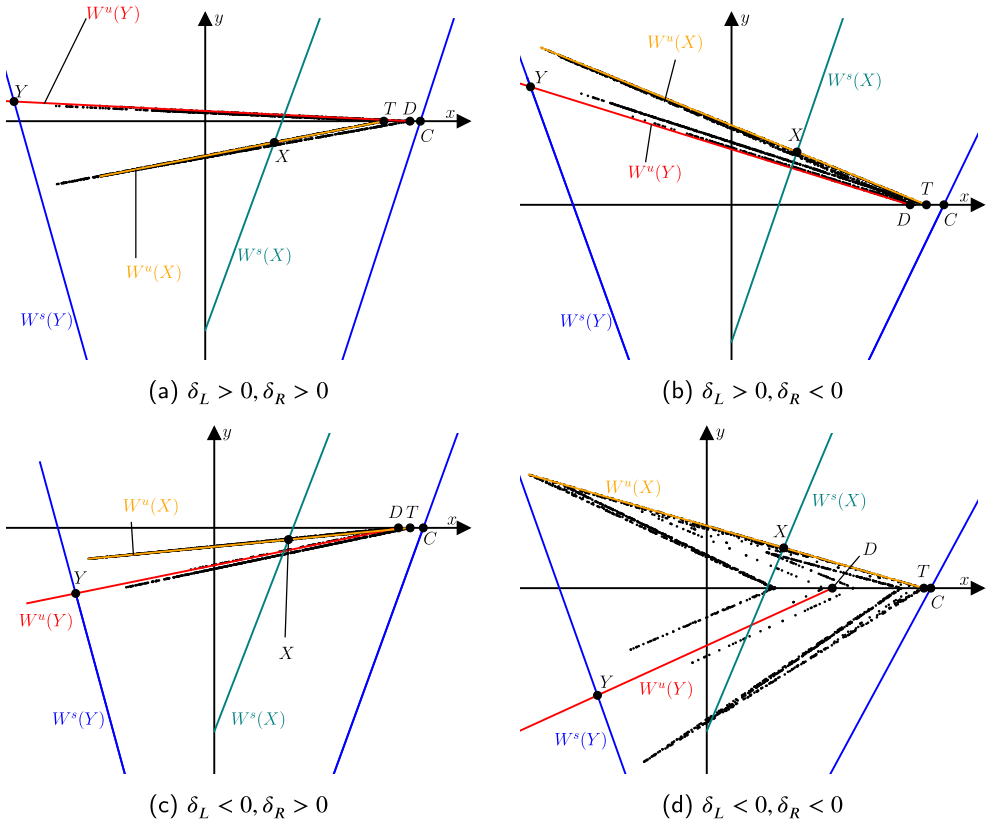

Fig. 3. Phase portraits of the BCNF (1) for four different parameter combinations: (a) $\xi = (2.1, 0.06, -1.7, 0.18)$; (b) $\xi = (2.1, 0.4, -1.7, -0.55)$; (c) $\xi = (2.2, -0.3, -1.7, 0.1)$; (d) $\xi = (1.8, -0.75, -1.6, -0.4)$. Each plot shows the linear segments of the stable and unstable manifolds emanating from the fixed points X and Y, as well as an adjoining segment of the stable manifold of Y. We also indicate some of their intersections with $y = 0$: T, D, and C; formulas for these are given by (11), (12), and (13). To illustrate the chaotic attractor the black dots show 2000 iterates of a typical forward orbit after transient dynamics has decayed.

A third point C will be also central to our later calculations. This point is where $W^s(Y)$, when grown outwards from Y to the right, first intersects $y = 0$ at a point with $x > 0$ and is given by

$$C = \left(\frac{{\lambda_L^u}^2}{(\delta_R - \tau_R \lambda_L^u)(\lambda_L^u - 1)}, 0 \right). \tag{13}$$

Fig. 3 indicates the points T, D, and C for four example phase portraits, one for each of the four cases for the signs of δ_L and δ_R. Notice if $\delta_L > 0$ (upper plots) the left half-plane maps to the upper half-plane, while if $\delta_L < 0$ (lower plots) the left half-plane maps to the lower half-plane. Similarly if $\delta_R > 0$ (left plots) the right half-plane maps to the lower half-plane, while if $\delta_R < 0$ (right plots) the right half-plane maps to the upper half-plane.

4. Renormalisation in two dimensions

In Section 2 we saw that renormalisation based on the substitution rule $(L, R) \mapsto (RR, LR)$ explains the bifurcation structure of the one-dimensional skew tent map family shown in Fig. 2. For the BCNF (1) this rule defines the renormalisation operator

$$g(\xi) = \left(\tau_R^2 - 2\delta_R, \delta_R^2, \tau_L \tau_R - \delta_L - \delta_R, \delta_L \delta_R \right). \tag{14}$$

The four values on the right-hand side of (14) are the traces and determinants of A_R^2 and $A_R A_L$. In this section we extend the basic aspects of this renormalisation operator beyond the orientation-preserving setting of our earlier work [13]. Renormalisation has also been applied to subfamilies of (1) by Pumariño et al. [31,32] and Ou [29].

We first identify the subset of Φ where the BCNF has a stable LR-cycle. Generalising (3) we have that the matrix $A_L A_R$ (whose eigenvalues are the stability multipliers of the LR-cycle) has an eigenvalue -1 when $\alpha(\xi) = 0$, where

$$\alpha(\xi) = \tau_L \tau_R + (\delta_L - 1)(\delta_R - 1). \tag{15}$$

If $\alpha(\xi) > 0$ this eigenvalue is greater than -1. For the LR-cycle to be stable we also need $\det(A_L A_R) < 1$, where $\det(A_L A_R) = \delta_L \delta_R$, so we define

$$\mathcal{P}_2 = \left\{ \xi \in \boldsymbol{\Phi} \,\middle|\, \delta_L \delta_R < 1,\ \alpha(\xi) > 0 \right\}. \tag{16}$$

Proposition 4.1. *If $\xi \in \mathcal{P}_2$ then f_ξ has an asymptotically stable LR-cycle.*

Proof. Let $\tilde{\tau}_R = \tau_L \tau_R - \delta_L - \delta_R$ and $\tilde{\delta}_R = \delta_L \delta_R$ be the trace and determinant of $A_L A_R$. All eigenvalues of $A_L A_R$ have modulus less than 1 if and only if $\tilde{\delta}_R < 1$ and $-\tilde{\delta}_R - 1 < \tilde{\tau}_R < \tilde{\delta}_R + 1$. Certainly $\tilde{\delta}_R < 1$ by assumption, and $-\tilde{\delta}_R - 1 < \tilde{\tau}_R$ by the definition of α; also

$$\tilde{\tau}_R - \tilde{\delta}_R - 1 = \tau_L \tau_R - (\delta_L + 1)(\delta_R + 1) < -|(\delta_L + 1)(\delta_R + 1)| - (\delta_L + 1)(\delta_R + 1) \le 0$$

by the definition of $\boldsymbol{\Phi}$.

The composed map $f_R \circ f_L$ is affine with unique fixed point

$$P = \frac{-1}{\tilde{\tau}_R - \tilde{\delta}_R - 1} \big(\tau_R + \delta_R + 1, -\delta_R(\tau_L + \delta_L + 1) \big).$$

Let

$$Q = f_L(P) = \frac{-1}{\tilde{\tau}_R - \tilde{\delta}_R - 1} \big(\tau_L + \delta_L + 1, -\delta_L(\tau_R + \delta_R + 1) \big).$$

Notice the first component of P is negative while the first component of Q is positive, thus $\{P, Q\}$ is a periodic solution of f_ξ. Above we showed all eigenvalues of $A_L A_R$ have modulus less than 1, hence $\{P, Q\}$ is asymptotically stable. □

If $\alpha(\xi) < 0$ the LR-cycle is unstable. This is always the case if $\delta_L + \delta_R \ge 0$:

Proposition 4.2. *If $\xi \in \boldsymbol{\Phi}$ with $\delta_L + \delta_R \ge 0$ then $\alpha(\xi) < 0$.*

Proof. Suppose $\xi \in \boldsymbol{\Phi}$ with $\delta_L + \delta_R \ge 0$. If $\delta_L, \delta_R \ge -1$ then

$$\alpha(\xi) < -(\delta_L + 1)(\delta_R + 1) + (\delta_L - 1)(\delta_R - 1) = -2(\delta_L + \delta_R) \le 0,$$

using the definition of $\boldsymbol{\Phi}$ in the first inequality. If instead $\delta_L < -1$ or $\delta_R < -1$ then $\delta_L \delta_R < -1$ because $\delta_L + \delta_R > 0$, so

$$\alpha(\xi) < (\delta_L + 1)(\delta_R + 1) + (\delta_L - 1)(\delta_R - 1) = 2(\delta_L \delta_R + 1) < 0. \quad \square$$

Now we show that if $\alpha(\xi) < 0$ then the renormalisation operator g produces another instance of the BCNF in $\boldsymbol{\Phi}$.

Proposition 4.3. *If $\xi \in \boldsymbol{\Phi}$ and $\alpha(\xi) < 0$ then $g(\xi) \in \boldsymbol{\Phi}$.*

Proof. Let $\tilde{\tau}_L = \tau_R^2 - 2\delta_R$, let $\tilde{\delta}_L = \delta_R^2$, and let $\tilde{\tau}_R$ and $\tilde{\delta}_R$ be as in the proof of Proposition 4.1; then $g(\xi) = \big(\tilde{\tau}_L, \tilde{\delta}_L, \tilde{\tau}_R, \tilde{\delta}_R\big)$. Observe $\tilde{\tau}_L - \tilde{\delta}_L - 1 = \tau_R^2 - (\delta_R + 1)^2 > 0$ because $\tau_R < -(\delta_R + 1)$, and $\tilde{\tau}_L + \tilde{\delta}_L + 1 = \tau_R^2 + (\delta_R + 1)^2 > 0$ because $\tau_R < 0$, thus $\tilde{\tau}_L > |\tilde{\delta}_L + 1|$. Also $\tilde{\tau}_R - \tilde{\delta}_R - 1 = \tau_L \tau_R - (\delta_L + 1)(\delta_R + 1) < 0$ because $\tau_L > \delta_L + 1$ and $\tau_R < \delta_R + 1$, and $\tilde{\tau}_R + \tilde{\delta}_R + 1 = \alpha(\xi) < 0$, by assumption, thus $\tilde{\tau}_R < -|\tilde{\delta}_R + 1|$. □

Now let

$$\Pi_\xi = \left\{ f_\xi^{-1}(x, y) \,\middle|\, x \ge 0 \right\}, \tag{17}$$

be the set of all points that map to the right half-plane. On Π_ξ the second iterate f_ξ^2 has only two pieces:

$$f_\xi^2(x, y) = \begin{cases} \big(f_{R,\xi} \circ f_{L,\xi} \big)(x, y), & x \le 0, \\ f_{R,\xi}^2(x, y), & x \ge 0. \end{cases} \tag{18}$$

For any $\xi \in \boldsymbol{\Phi}$ (18) is affinely conjugate to $f_{g(\xi)}$. Specifically $f_\xi^2 = h_\xi^{-1} \circ f_{g(\xi)} \circ h_\xi$ on Π_ξ, where

$$h_\xi(x, y) = \frac{1}{\tau_R + \delta_R + 1} \begin{bmatrix} x \\ \delta_R x + \tau_R y - \delta_R \end{bmatrix}, \tag{19}$$

is the necessary change of coordinates. As an example Fig. 4-a shows Π_ξ (in the phase space of f_ξ) at the parameter point

$$\xi_{\text{ex}}^{(1)} = (1.5, 0.4, -1.5, 0.4), \tag{20}$$

while Fig. 4-b shows $h_\xi(\Pi_\xi)$ (in the phase space of $f_{g(\xi)}$). The map $f_{g(\xi)}$ has an invariant set $\Lambda \subset h_\xi(\Pi_\xi)$, so, as shown below, $h_\xi^{-1}(\Lambda) \subset \Pi_\xi$ is an invariant set of f_ξ^2. Moreover, the union of $h_\xi^{-1}(\Lambda)$ and its image under f_ξ is an invariant set of f_ξ. It is easy to infer the number of connected components in this set from the number of connected components of Λ, and this forms the basis of the renormalisation scheme.

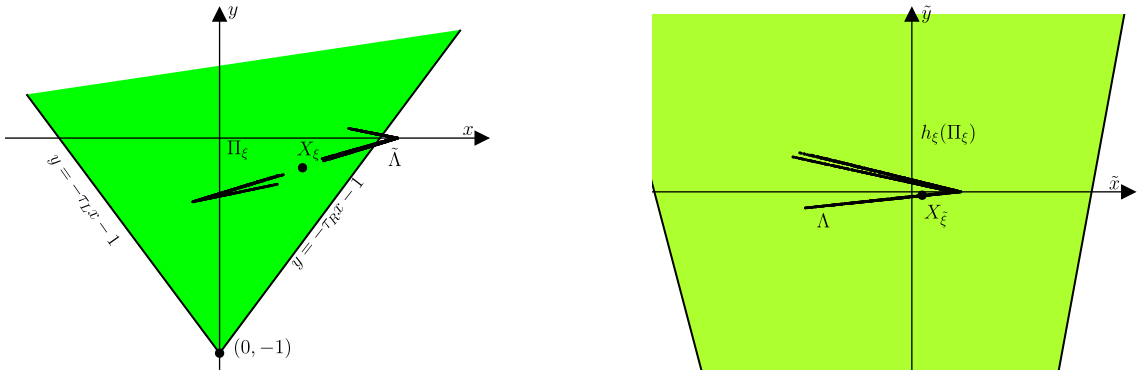

(a) $\xi = \xi_{\text{ex}}^{(1)} \in \mathcal{R}_1^{(1)}$ (b) $\xi = g\left(\xi_{\text{ex}}^{(1)}\right) \in \mathcal{R}_0^{(1)}$

Fig. 4. Phase portraits of the BCNF (1). Panel (a) uses the example parameter point $\xi_{\text{ex}}^{(1)}$ given by (20) where the attracor $\tilde{\Lambda}$ has two connected components, one of which lies entirely in Π_ξ (shaded). Panel (b) uses the parameter point $g\left(\xi_{\text{ex}}^{(1)}\right)$ where the attractor Λ has one connected component in $h_\xi(\Pi_\xi)$ (shaded).

Proposition 4.4. *Suppose $\Lambda \subset h_\xi(\Pi_\xi)$ is an invariant set of $f_{g(\xi)}$. Then $\tilde{\Lambda} = h_\xi^{-1}(\Lambda) \cup f_\xi\left(h_\xi^{-1}(\Lambda)\right)$ is an invariant set of f_ξ. Moreover, if $h_\xi^{-1}(\Lambda) \cap f_\xi\left(h_\xi^{-1}(\Lambda)\right) = \varnothing$ then the number of connected components of $\tilde{\Lambda}$ is twice the number of connected components of Λ.*

Proof. Let $S = h_\xi^{-1}(\Lambda)$. Since $S \subset \Pi_\xi$,

$$f_\xi^2(S) = h_\xi^{-1}\left(f_{g(\xi)}\left(h_\xi(S)\right)\right). \tag{21}$$

But $h_\xi(S) = \Lambda$ and $f_{g(\xi)}(\Lambda) = \Lambda$, so the right-hand side of (21) is $h_\xi^{-1}(\Lambda) = S$. Thus S is invariant under f_ξ^2, so $S \cup f_\xi(S)$ is invariant under f_ξ. Since h_ξ is invertible the number of components of S is the same as the number of components of Λ. If $S \cap f_\xi(S) = \varnothing$ then $f_\xi(S)$ also has this many components (for otherwise $f_\xi^2(S) = S$ would not be possible because f_ξ is continuous). □

5. The orientation-preserving case

In this section we summarise the main results of our earlier work [13]. Let

$$\Phi^{(1)} = \left\{ \xi \in \Phi \;\middle|\; \delta_L > 0, \delta_R > 0 \right\}, \tag{22}$$

be the subset of Φ for which the BCNF is orientation-preserving. In a large part of $\Phi^{(1)}$ an attractor is destroyed when the points C and D (shown in Fig. 3-a) coincide. This is a homoclinic bifurcation, or homoclinic corner [37], where the stable and unstable manifolds of the fixed point Y attain non-trivial intersections. Straight-forward algebra gives

$$C_1 - D_1 = \frac{\phi^+(\xi)}{(\lambda_L^u - 1)(1 - \lambda_L^s)(\delta_R - \tau_R \lambda_L^u)}, \tag{23}$$

where

$$\phi^+(\xi) = \delta_R - (\tau_R + \delta_L + \delta_R - (1 + \tau_R)\lambda_L^u)\lambda_L^u. \tag{24}$$

Fig. 5 shows an example. In panel (a) the closure of the unstable manifold of X,

$$\Lambda = \text{cl}(W^u(X)), \tag{25}$$

is a chaotic attractor. As the value of τ_L is increased the attractor approaches the point D and is destroyed at $\tau_L \approx 1.9083$ when $\phi^+(\xi) = 0$, panel (b). At larger values of τ_L almost all forward orbits diverge, panel (c).

In some parts of $\Phi^{(1)}$ the attractor Λ is not destroyed at $\phi^+(\xi) = 0$. This occurs when it does not approach D as $C \to D$; instead the attractor is destroyed in a subsequent heteroclinic bifurcation involving a period-three solution [12].

With $\delta_L = \delta_R = 0$ we have $\phi^+(\xi) = \tau_L \phi_0(\tau_L, \tau_R)$, so in this case the bifurcation surface $\phi^+(\xi) = 0$ reduces to the homoclinic bifurcation $\phi_0(\tau_L, \tau_R) = 0$ of the skew tent map family. This motivates the definition

$$\mathcal{R}_n^{(1)} = \left\{ \xi \in \Phi^{(1)} \;\middle|\; \phi^+(g^n(\xi)) > 0,\ \phi^+(g^{n+1}(\xi)) \le 0 \right\}, \tag{26}$$

for all $n \ge 0$. The constraint $\alpha(\xi) < 0$ is not needed in this definition because, by Proposition 4.2, if $\xi \in \Phi^{(1)}$ then automatically $\alpha(\xi) < 0$. As shown in [13] the regions $\mathcal{R}_n^{(1)}$ are disjoint and cover the subset of $\Phi^{(1)}$ for which $\phi^+(\xi) > 0$. These regions are more

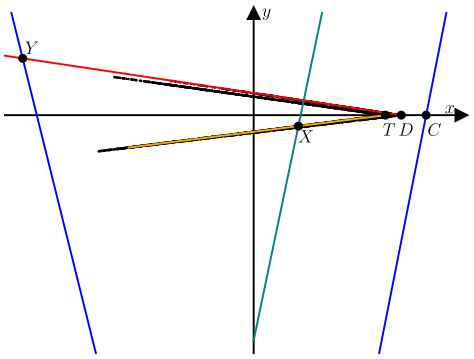

(a) $\tau_L = 1.7$

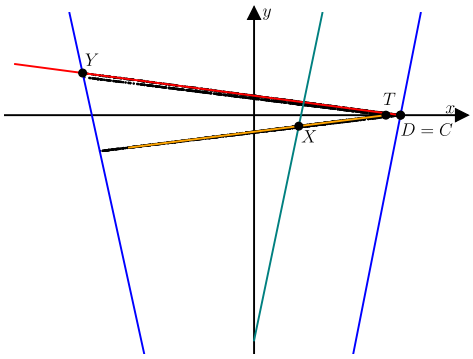

(b) $\tau_L \approx 1.9083$

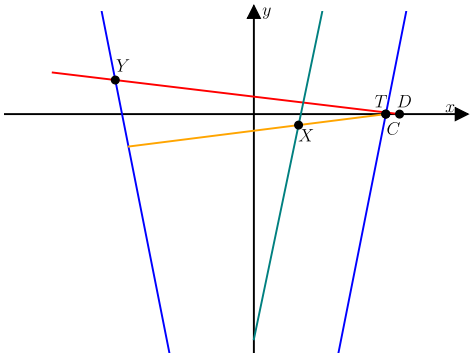

(c) $\tau_L = 2.1$

Fig. 5. Phase portraits of (1) with $\delta_L = 0.1$, $\delta_R = 0.1$, $\tau_R = -2$ and three different values of τ_L. These parameter values correspond to the black triangles in Fig. 6-a. Panel (b) uses τ_L such that $\phi^+(\xi) = 0$ to ten decimal places. In (a) $\mathrm{cl}(W^u(X))$ is a chaotic attractor; in (b) $W^s(Y)$ and $W^u(Y)$ form a homoclinic corner by intersecting at $D = C$; in (c) there is no attractor.

difficult to visualise than those in Section 2 because they are four-dimensional. Fig. 6 shows two-dimensional slices of parameter space defined by fixing $\delta_L > 0$ and $\delta_R > 0$. In these slices only finitely many $\mathcal{R}_n^{(1)}$ are visible because as $n \to \infty$ they converge to $\xi = (1, 0, -1, 0)$ (a fixed point of g). The following result describes Λ for parameter values in $\mathcal{R}_0^{(1)}$. For a proof see [13].

Theorem 5.1. *For any $\xi \in \mathcal{R}_0^{(1)}$,*

(i) Λ is bounded, connected, and invariant under f_ξ,
(ii) has a positive Lyapunov exponent, and
(iii) if $\delta_R < 1$ there exists a forward invariant set $\Delta \subset \mathbb{R}^2$ with non-empty interior such that

$$\bigcap_{n=0}^{\infty} f_\xi^n(\Delta) = \Lambda. \tag{27}$$

Item (ii) says Λ is chaotic in the sense of having a positive Lyapunov exponent. We believe it satisfies Devaney's definition of chaos throughout $\Phi^{(1)}$, but have only proved this in a subset of $\Phi^{(1)}$ [12]. Item (iii) says Λ is a Milnor attractor. We believe the condition $\delta_R > 1$ is unnecessary and Λ is in fact a topological attractor throughout $\mathcal{R}_0^{(1)}$.

To understand the dynamics in all other regions $\mathcal{R}_n^{(1)}$ we use the renormalisation operator g. The following result follows simply from Proposition 4.3 and the definition of $\mathcal{R}_n^{(1)}$.

Proposition 5.2. *If $\xi \in \mathcal{R}_n^{(1)}$ with $n \geq 1$, then $g(\xi) \in \mathcal{R}_{n-1}^{(1)}$.*

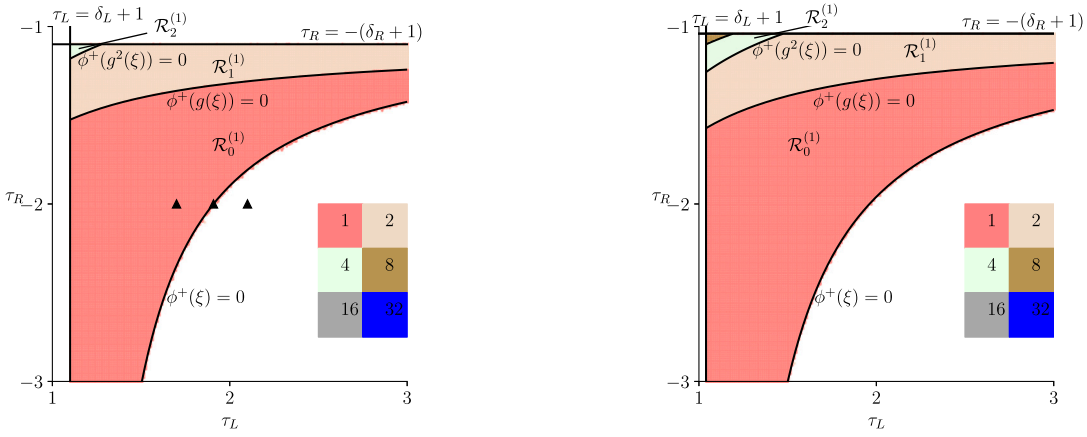

(a) $\delta_L = 0.1, \delta_R = 0.1$. (b) $\delta_L = 0.04, \delta_R = 0.04$.

Fig. 6. Two-dimensional slices of the orientation-preserving parameter region $\Phi^{(1)}$ showing the curves $\phi(g^n(\xi)) = 0$, for low values of n, overlaid upon the numerical results of Eckstein's greatest common divisor algorithm, explained in Section 6. Each point in a 200 × 200 grid is coloured by the greatest common divisor of a set of close return iteration numbers J according to the colour bar on the right. In the algorithm we used $\varepsilon = 0.001$ and $M = 10^6$; also points are coloured white if iterates appeared to diverge. The black triangles correspond to the parameter values of Fig. 5.

So if $\xi \in \mathcal{R}_n^{(1)}$ then $g^n(\xi) \in \mathcal{R}_0^{(1)}$ where the attractor is connected. Then by n applications of Proposition 4.4, f_ξ has an attractor with 2^n connected components as long as the assumptions of Proposition 4.4 are satisfied in each application. This is indeed the case, as shown in [13] through a series of careful calculations, and gives the following result.

Theorem 5.3. *For any $\xi \in \mathcal{R}_n^{(1)}$ with $n \geq 0$, f_ξ has a chaotic Milnor attractor with exactly 2^n connected components.*

For example Fig. 4-a uses $\xi = \xi_{\text{ex}}^{(1)}$ belonging to $\mathcal{R}_1^{(1)}$ so the attractor has two connected components, as shown. The renormalisation allows us to say more about this attractor. Specifically each piece of the attractor is an affine transformation of the one-component attractor of (1) with $\xi = g\left(\xi_{\text{ex}}^{(1)}\right)$ belonging to $\mathcal{R}_0^{(1)}$, shown in Fig. 4-b.

6. A component counting algorithm

To support an extension of the theoretical results of Section 5 to the orientation-reversing and non-invertible settings, we perform numerical simulations to count the number of connected components of the attractors. There are many methods for estimating the number of connected components of a set Ψ from a finite collection F of points in Ψ. For example Robins et al. [34] connect all pairs of points in F with line segments to form a complete graph, then base their estimation from a minimal spanning tree. In our setting Ψ is generated by a map, so it is more effective to use a method that utilises the dynamics. For this reason we compute the number of components as the greatest common divisor of a certain set of computed values. This method originates with Eckstein [9] and is described by Avrutin et al. [1]. As explained at the end of this section, the effectiveness of the method relies on the following result.

Lemma 6.1. *Suppose a compact invariant set Ψ of a continuous map f has $k \geq 2$ connected components, and f has an orbit that visits all components. Then the components can be labelled as $\Psi_1, \Psi_2, \ldots, \Psi_k$ such that $f(\Psi_1) = \Psi_2, f(\Psi_2) = \Psi_3, \ldots, f(\Psi_{k-1}) = \Psi_k$, and $f(\Psi_k) = \Psi_1$.*

Thus the components of Ψ are ordered cyclically, each has one 'predecessor' and one 'successor'. The following proof is adapted from [1,9]. It uses a small quantity ε to avoid reference to path-connectedness.

Proof of Lemma 6.1. By assumption there exists $P \in \Psi$ whose forward orbit enters all components. Let Ψ_1 be the component containing P. Suppose for a contradiction $f(\Psi_1)$ contains points in two different components, T and U. Since Ψ is compact there exists $d > 0$ such that any point in T and any point in U are at least a distance d apart. Since Ψ_1 is connected for any $\varepsilon > 0$ there exist $Q, R \in \Psi_1$ with $\|Q - R\| < \varepsilon$ such that $f(Q) \in T$ and $f(R) \in U$. But $\|f(Q) - f(R)\| > d$ so this is not possible because f is continuous, hence $f(\Psi_1)$ is a subset of one component of Ψ. This component is not Ψ_1 (because then Ψ_1 would be forward invariant and the forward orbit of P could not reach the other components), let us call it Ψ_2. So $f(\Psi_1) \subset \Psi_2$.

By a similar argument $f(\Psi_2)$ is a subset of one component, and if $k > 2$ this component is neither Ψ_1 nor Ψ_2, call it Ψ_3. Inductively we obtain $\Psi_1, \Psi_2, \ldots, \Psi_k$ with $f(\Psi_1) \subset \Psi_2, f(\Psi_2) \subset \Psi_3, \ldots, f(\Psi_{k-1}) \subset \Psi_k$. Also $f(\Psi_k)$ is a subset of one component.

But Ψ is invariant, meaning $f(\Psi) = \Psi$. Thus $f(\Psi_k) \subset \Psi_1$, and further $f(\Psi_1) = \Psi_2, f(\Psi_2) = \Psi_3, \ldots, f(\Psi_{k-1}) = \Psi_k$, and $f(\Psi_k) = \Psi_1$ as required. □

Now fix ξ and suppose f_ξ has an attractor Λ with $k \geq 1$ connected components. To compute the value k, which is assumed to be unknown to us *a priori*, the algorithm proceeds as follows. Fix $\varepsilon > 0$ (we used $\varepsilon = 0.001$ or $\varepsilon = 0.0001$) and $M > 0$ (we used $M = 10^6$) and let $J = \varnothing$. Choose some initial point assumed to be in the basin of attraction of Λ and iterate it under f_ξ a reasonably large number of times (we used 10^4 iterations) to remove transient dynamics and obtain a point in Λ, or extremely close to Λ, call it (x_0, y_0). Iterate further, and for all $i = 1, 2, \ldots, M$ evaluate the distance (Euclidean norm in $\mathbb{R}^2$) between $f_\xi^i(x_0, y_0)$ and (x_0, y_0). If this distance is less than ε, append the number i to the set J. Finally evaluate the greatest common divisor of the elements in J — this is our estimate for the value of k.

For example using $\xi = \xi_{\text{ex}}^{(1)}$, as in Fig. 4-a, the algorithm generated a set of 1249 numbers

$$J = \{1292, 3170, 3778, \ldots, 999930\},$$

whose elements have greatest common divisor 2 (and indeed at this parameter point the attractor has two components).

Fig. 6 shows the output of this algorithm over a 200×200 grid of parameter points. The results show excellent agreement to the theory described in Section 5. For example parameter points where the greatest common divisor of the numbers in J is two have boundaries indistinguishable from the true bifurcation boundaries $\phi(g(\xi)) = 0$ and $\phi(g^2(\xi)) = 0$.

Two principles underlie the effectiveness of the algorithm. First, if the distance between any two components of Λ is greater than ε, then $\left\| f_\xi^i(x_0, y_0) - (x_0, y_0) \right\| < \varepsilon$ implies that $f_\xi^i(x_0, y_0)$ and (x_0, y_0) belong to the same component of Λ (assuming $(x_0, y_0) \in \Lambda$). By Lemma 6.1 this is only possible if i is a multiple of k. Thus the elements of J are all multiples of k.

Second, assuming f_ξ is ergodic on Λ, the set of all $i > 0$ giving $\left\| f_\xi^i(x_0, y_0) - (x_0, y_0) \right\| < \varepsilon$ will not be expected to share a multiple larger than k. This is because ergodicity implies the dynamics of f_ξ^k on any component are well mixed (see Haydn et al. [15] and references within for theory on the probability distribution of the values of i when ε is small). In our setting $M = 10^6$ seems to generate large enough sets J to ensure the greatest common divisor of the numbers in J is k, instead a multiple of k. One can also modify the algorithm, as described in [1,9], to search for a close return to several reference points, instead of the single point (x_0, y_0).

7. The orientation-reversing case

Let

$$\boldsymbol{\Phi}^{(2)} = \left\{ \xi \in \boldsymbol{\Phi} \;\middle|\; \delta_L < 0, \delta_R < 0 \right\}, \tag{28}$$

be the subset of $\boldsymbol{\Phi}$ for which the BCNF is orientation-reversing. As shown originally by Misiurewicz [25], the closure of the unstable manifold of the fixed point X can be a chaotic attractor. This attractor contains the point T, as shown in Fig. 3-d, so under parameter variation is destroyed when $T = C$. This is a heteroclinic bifurcation beyond which the unstable manifold of X is unbounded. From the formulas (11) and (13) we obtain

$$C_1 - T_1 = \frac{\phi^-(\xi)}{(\lambda_L^u - 1)(1 - \lambda_R^s)(\delta_R - \tau_R \lambda_L^u)}, \tag{29}$$

where

$$\phi^-(\xi) = \delta_R - (\delta_R + \tau_R - (1 + \lambda_R^u)\lambda_L^u)\lambda_L^u. \tag{30}$$

An example illustrating the destruction of the attractor is shown in Fig. 7. As the value of τ_L is increased the attractor is destroyed when $T = C$ at $\tau_L \approx 2.0104$.

Analogous to the orientation-preserving case, if $\delta_L = \delta_R = 0$ the expression $\phi^-(\xi)$ reduces to $\phi^-(\xi) = \tau_L \phi_0(\tau_L, \tau_R)$. Thus the heteroclinic bifurcation $\phi^-(\xi) = 0$ reduces to the familiar homoclinic bifurcation $\phi_0(\tau_L, \tau_R) = 0$ of the skew tent map family in the limit $(\delta_L, \delta_R) \to (0, 0)$.

We are now ready to subdivide $\boldsymbol{\Phi}^{(2)}$ into regions based upon the renormalisation operator g, (14). But $\xi \in \boldsymbol{\Phi}^{(2)}$ implies $g(\xi) \in \boldsymbol{\Phi}^{(1)}$, so we again use the preimages of $\phi^+(\xi) = 0$ under g to define the region boundaries. Specifically we let

$$\mathcal{R}_0^{(2)} = \left\{ \xi \in \boldsymbol{\Phi}^{(2)} \;\middle|\; \phi^-(\xi) > 0, \phi^+(g(\xi)) \leq 0, \alpha(\xi) < 0 \right\}, \tag{31}$$

$$\mathcal{R}_n^{(2)} = \left\{ \xi \in \boldsymbol{\Phi}^{(2)} \;\middle|\; \phi^+\left(g^n(\xi)\right) > 0, \phi^+\left(g^{n+1}(\xi)\right) \leq 0, \alpha(\xi) < 0 \right\}, \qquad \text{for all } n \geq 1. \tag{32}$$

Fig. 8 shows these regions in two typical two-dimensional slices of parameter space. Unlike in the orientation-preserving setting we need to impose $\alpha(\xi) < 0$ in these regions so that they do not overlap $\mathcal{P}_2$ where a stable LR-cycle exists.

We conjecture that throughout $\mathcal{R}_0^{(2)}$ the map has a unique chaotic attractor with one connected component equal to the closure of the unstable manifold of X, as in Fig. 7-a. In earlier work [11] we proved this to be true on a subset of $\mathcal{R}_0^{(2)}$. In the special case $\tau_L = -\tau_R$ and $\delta_L = \delta_R$ of the Lozi family of maps, the constraint $\phi^-(\xi) > 0$ reduces to equation (3) of Misiurewicz [25].

The following result is a simple consequence of Propositions 4.2 and 4.3 and (32).

Proposition 7.1. *If $\xi \in \mathcal{R}_n^{(2)}$ with $n \geq 1$, then $g(\xi) \in \mathcal{R}_{n-1}^{(1)}$.*

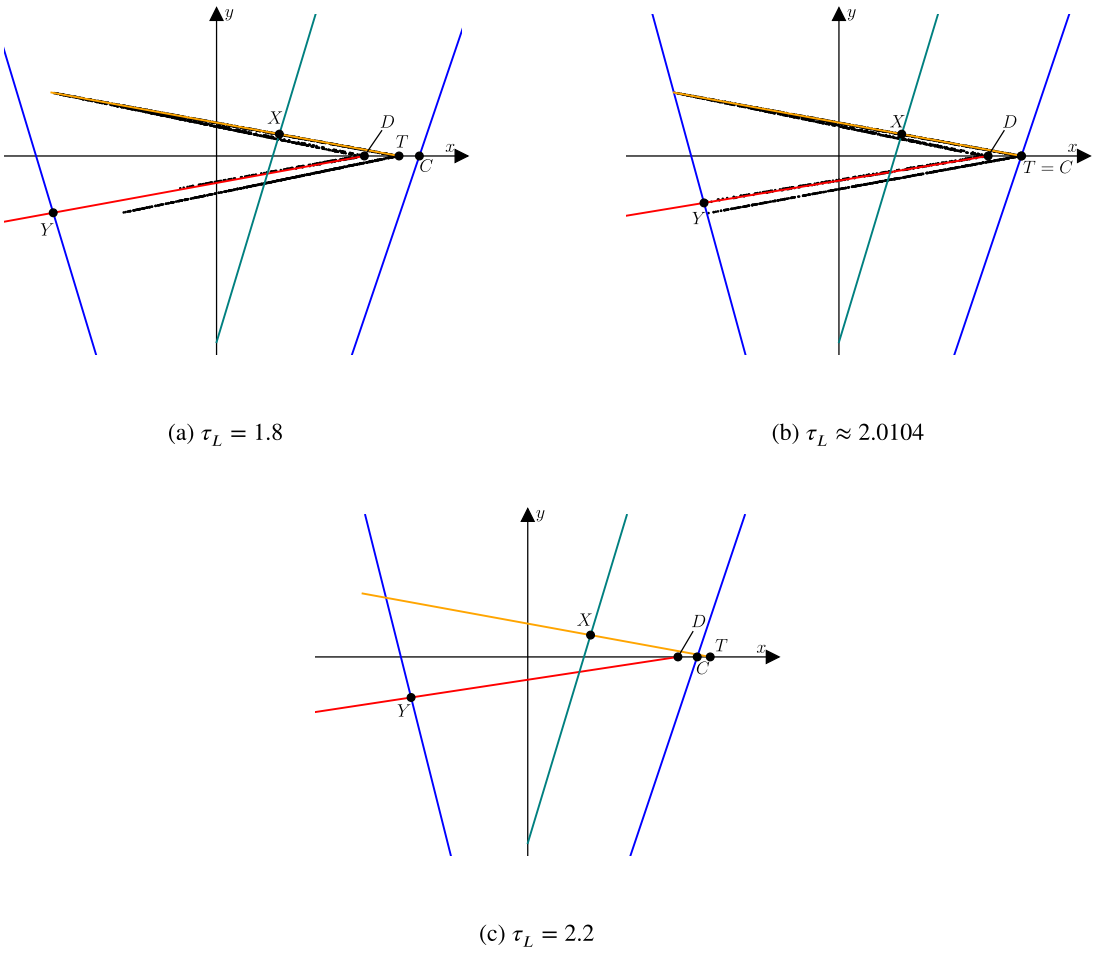

(a) $\tau_L = 1.8$ (b) $\tau_L \approx 2.0104$

(c) $\tau_L = 2.2$

Fig. 7. Phase portraits of Eq. (1) with $\delta_L = -0.2$, $\delta_R = -0.2$, $\tau_R = -1.8$, and three different values of τ_L corresponding to the black triangles in Fig. 8-b. Panel (b) uses τ_L such that $\phi^-(\xi) = 0$ to ten decimal places. In (a) $\mathrm{cl}(W^u(X))$ is a chaotic attractor; in (b) $W^u(X)$ and $W^s(Y)$ have corner intersections; in (c) there is no attractor.

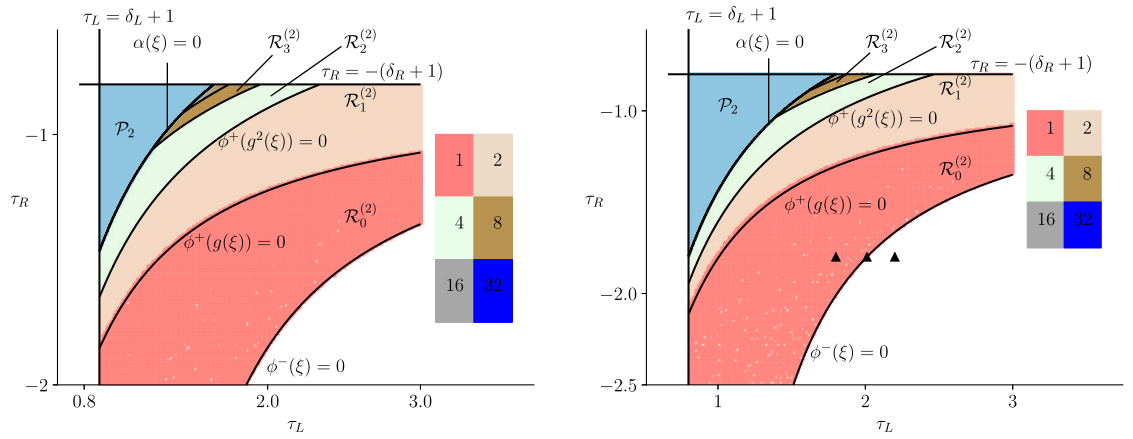

(a) $\delta_L = -0.1, \delta_R = -0.2.$ (b) $\delta_L = -0.2, \delta_R = -0.2.$

Fig. 8. Two-dimensional slices of the orientation-reversing parameter region $\Phi^{(2)}$ showing the bifurcation curves overlaid upon numerical results obtained using $\epsilon = 0.0001$ and $M = 10^6$. The black triangles correspond to the parameter values of Fig. 7.

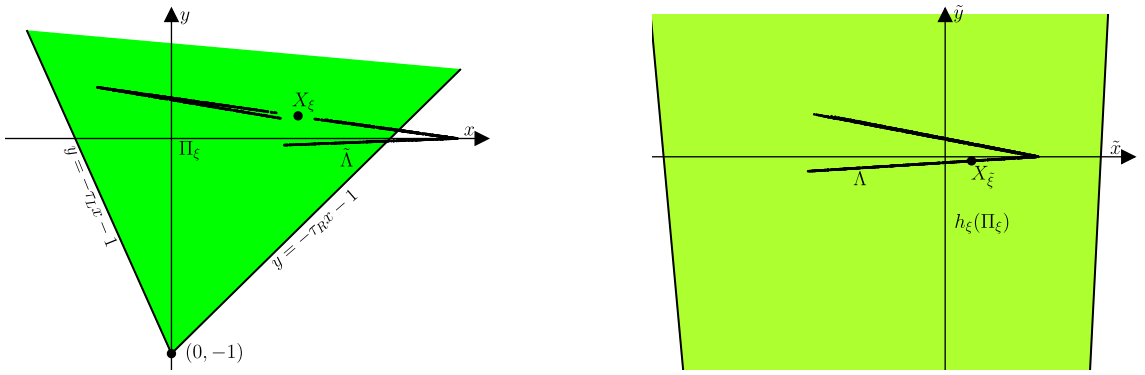

(a) $\xi = \xi_{\text{ex}}^{(2)} \in \mathcal{R}_1^{(2)}$ (b) $\xi = g\left(\xi_{\text{ex}}^{(2)}\right) \in \mathcal{R}_0^{(1)}$

Fig. 9. Panel (a) is a phase portrait of (1) at the parameter point $\xi_{\text{ex}}^{(2)}$ (33) where the attractor has two connected components in the orientation-reversing case. Panel (b) uses instead $g\left(\xi_{\text{ex}}^{(2)}\right)$.

This suggests that for any $\xi \in \mathcal{R}_n^{(2)}$ the BCNF has an attractor with 2^n connected components. For example

$$\xi_{\text{ex}}^{(2)} = (2.5, -0.1, -1.1, -0.2) \tag{33}$$

belongs to $\mathcal{R}_1^{(2)}$ and indeed the attractor shown in Fig. 9-a appears to have two connected components. One component belongs to Π_ξ so Proposition 4.4 applies. Hence this component is an affine transformation of the attractor of (1) at the parameter point $g\left(\xi_{\text{ex}}^{(2)}\right)$ that belongs to $\mathcal{R}_0^{(1)}$, and we know its attractor has one component by Theorem 5.1.

Fig. 8 shows that our conjecture is supported by the output of the greatest common divisor algorithm. The boundaries of the $\mathcal{R}_n^{(2)}$ closely approximate the places with the value of the greatest common divisor changes. This value changes slightly above $\phi^+(g(\xi)) = 0$ because here the two components of the attractor are very close and $\varepsilon = 0.0001$ is insufficient to detect this difference. Also $\mathcal{R}_0^{(2)}$ has pixels erroneously corresponding to more than one component because here the attractor is relatively large and $M = 10^6$ iterations are insufficient for the algorithm to consistently obtain a greatest common divisor of 1.

8. The non-invertible case $\delta_L > 0$, $\delta_R < 0$

Here we study the parameter region

$$\boldsymbol{\Phi}^{(3)} = \left\{ \xi \in \boldsymbol{\Phi} \;\middle|\; \delta_L > 0, \delta_R < 0 \right\}, \tag{34}$$

where (1) is non-invertible. In this region an attractor of (1) can be destroyed by crossing the homoclinic bifurcation $\phi^+(\xi) = 0$ or the heteroclinic bifurcation $\phi^-(\xi) = 0$. This is because near these boundaries the attractor contains the point T and is close to the point D so is destroyed when one of these points collides with C. For example in Fig. 10 T lies to the left of D, so the attractor is destroyed when $D = C$, i.e. when $\phi^+(\xi) = 0$. In contrast in Fig. 11 T lies to the right of D, so the attractor is destroyed when $T = C$, i.e. when $\phi^-(\xi) = 0$. For this reason we define

$$\phi_{\min}(\xi) = \min[\phi^+(\xi), \phi^-(\xi)], \tag{35}$$

and

$$\mathcal{R}_n^{(3)} = \left\{ \xi \in \boldsymbol{\Phi}^{(3)} \;\middle|\; \phi_{\min}\left(g^n(\xi)\right) > 0,\ \phi_{\min}\left(g^{n+1}(\xi)\right) \le 0,\ \alpha(\xi) < 0 \right\}, \tag{36}$$

for all $n \ge 0$. Two-dimensional slices of these regions are shown in Fig. 12. We conjecture that throughout the first region $\mathcal{R}_0^{(3)}$ the BCNF has a unique chaotic attractor with one connected component, and this is supported by the numerical results shown in Fig. 12. To explain the dynamics in the remaining regions we use the following analogy to Propositions 5.2 and 7.1. Here, however, the result is not trivial, so we provide a proof.

Proposition 8.1. *If $\xi \in \mathcal{R}_n^{(3)}$ with $n \ge 1$, then $g(\xi) \in \mathcal{R}_{n-1}^{(3)}$.*

Proof. Choose any $\xi \in \mathcal{R}_n^{(3)}$ with $n \ge 1$ and write $g(\xi) = \left(\tilde{\tau}_L, \tilde{\delta}_L, \tilde{\tau}_R, \tilde{\delta}_R\right)$ as in the proof of Proposition 4.3. By Proposition 4.3 we have $g(\xi) \in \boldsymbol{\Phi}$. Further, $g(\xi) \in \boldsymbol{\Phi}^{(3)}$ because $\tilde{\delta}_L = \delta_R^2 > 0$ and $\tilde{\delta}_R = \delta_L \delta_R < 0$. Also $\phi_{\min}\left(g^{n-1}(g(\xi))\right) > 0$ and $\phi_{\min}\left(g^n(g(\xi))\right) \le 0$. Finally

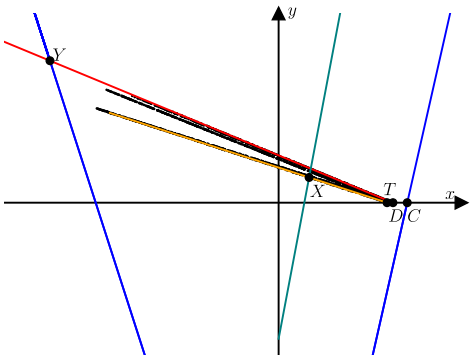

(a) $\tau_L = 1.7$

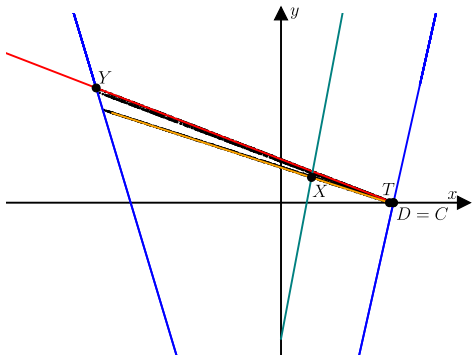

(b) $\tau_L \approx 1.7948$

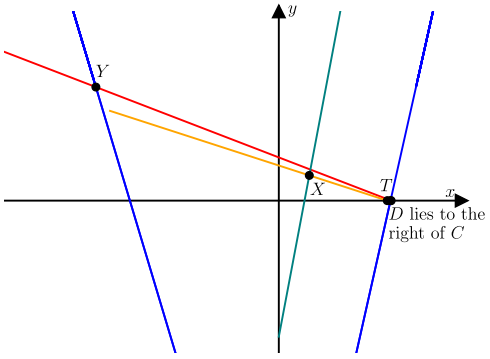

(c) $\tau_L = 1.8$

Fig. 10. Phase portraits of (1) with $\delta_L = 0.3$, $\delta_R = -0.4$, $\tau_R = -2.4$ and three different values of τ_L corresponding to the blue triangles in Fig. 12-b.

$\alpha(g(\xi)) = \tilde{\tau}_L\tilde{\tau}_R + (\tilde{\delta}_L - 1)(\tilde{\delta}_R - 1)$ where $\tilde{\tau}_L = \tau_R^2 - 2\delta_R$, $\tilde{\delta}_L = \delta_R^2$, $\tilde{\tau}_R = \tau_L\tau_R - \delta_L - \delta_R$, and $\tilde{\delta}_R = \delta_L\delta_R$. By substituting $\tau_L > \delta_L + 1$ and $\tau_R < -(\delta_R + 1)$ (true because $\xi \in \Phi$) we obtain (after simplification)

$$\alpha(g(\xi)) < -2\left(1 + \delta_R + \delta_R^2\right)(\delta_L + \delta_R).$$

So if $\delta_L + \delta_R > 0$ then $\alpha(g(\xi)) < 0$ (because $1 + \delta_R + \delta_R^2 \geq \frac{3}{4} > 0$). If instead $\delta_L + \delta_R \leq 0$ then $\tilde{\delta}_L + \tilde{\delta}_R = \delta_R(\delta_L + \delta_R) \geq 0$ because $\delta_R < 0$, so again $\alpha(g(\xi)) < 0$ by Proposition 4.2 applied to the parameter point $g(\xi)$. □

Proposition 8.1 suggests that throughout each $\mathcal{R}_n^{(3)}$ with $n \geq 1$ the BCNF has an attractor with exactly 2^n connected components, and Fig. 12 supports this conjecture. Fig. 13-a provides an example using the parameter point

$$\xi_{\text{ex}}^{(3)} = (3, 0.3, -.9, -0.4), \tag{37}$$

which belongs to $\mathcal{R}_1^{(3)}$. The attractor has two pieces, one of which belongs to Π_ξ, so as above this piece is an affine transformation of the attractor of $g\left(\xi_{\text{ex}}^{(3)}\right) \in \mathcal{R}_0^{(3)}$ shown in Fig. 13-b.

9. The non-invertible case $\delta_L < 0$, $\delta_R > 0$

It remains for us to consider

$$\Phi^{(4)} = \left\{\xi \in \Phi \;\middle|\; \delta_L < 0, \delta_R > 0\right\}, \tag{38}$$

where (1) is non-invertible. In this region the attractor is usually destroyed before the boundaries $\phi^+(\xi) = 0$ and $\phi^-(\xi) = 0$ in a heteroclinic bifurcation that cannot be characterised by an explicit condition on the parameter values. This occurs when the attractor contains points on $y = 0$ that lie to the right of D and T and is destroyed when its right-most point collides with C.

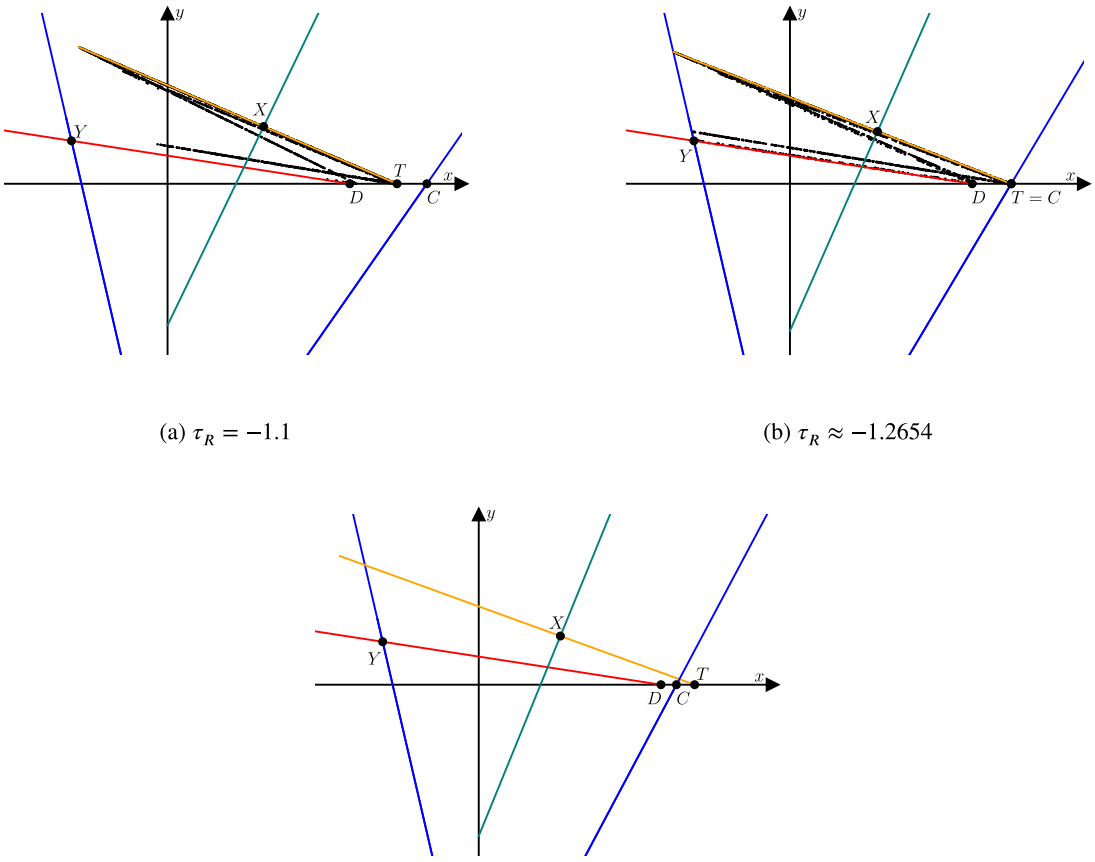

(a) $\tau_R = -1.1$ (b) $\tau_R \approx -1.2654$

(c) $\tau_R = -1.4$

Fig. 11. Phase portraits of (1) with $\delta_L = 0.3$, $\delta_R = -0.4$, $\tau_L = 3$, and three different values of τ_R corresponding to the black triangles in Fig. 12-b.

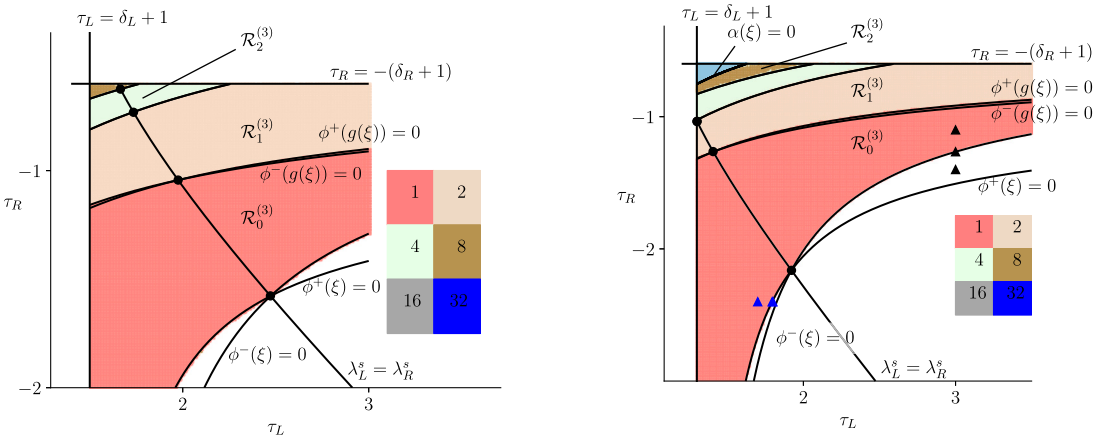

(a) $\delta_L = 0.5, \delta_R = -0.4$. (b) $\delta_L = 0.3, \delta_R = -0.4$.

Fig. 12. Two-dimensional slices of the non-invertible parameter region $\Phi^{(3)}$ showing the bifurcation curves overlaid upon numerical results obtained using $\epsilon = 0.001$ and $M = 10^6$. The blue [black] triangles correspond to the parameter values of Fig. 10 [Fig. 11].

Fig. 14 shows an example. In panel (a) the attractor is the closure of the unstable manifold of X. As we grow the unstable manifold outwards from X it develops points on $y = 0$ that lie further and further to the right, but not beyond C. This occurs as a

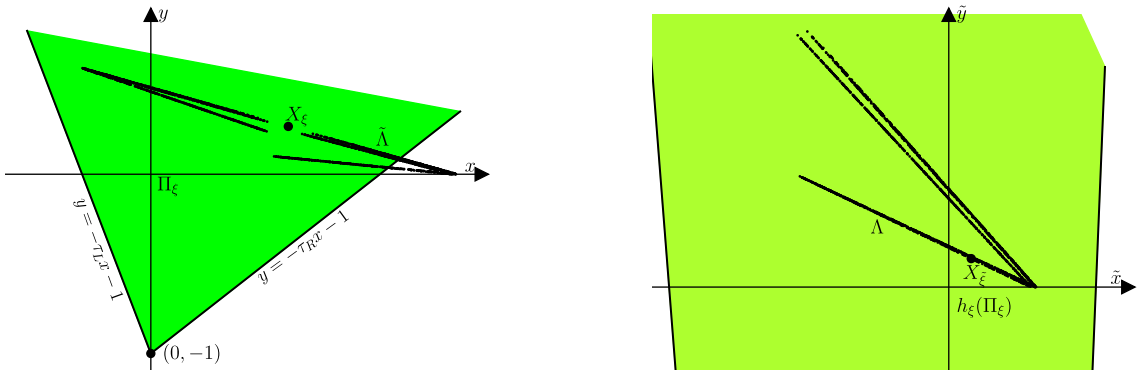

(a) $\xi = \xi_{\text{ex}}^{(3)} \in \mathcal{R}_1^{(3)}$ (b) $\xi = g\left(\xi_{\text{ex}}^{(3)}\right) \in \mathcal{R}_0^{(3)}$

Fig. 13. Panel (a) is a phase portrait of (1) at the parameter point $\xi_{\text{ex}}^{(3)}$ (37) where the attractor has two connected components in the $\delta_L > 0$ non-invertible case. Panel (b) uses instead $g\left(\xi_{\text{ex}}^{(3)}\right)$.

consequence of the geometric configuration afforded by f_R being orientation-preserving and f_L being orientation-reversing. As the value of τ_L is increased the attractor is destroyed when its right-most point collides with C, panel (b). With a slightly value of τ_L, panel (c), typical forward orbits diverge even though D and T still lie to the left of C. Fig. 15 provides a second example. Here the parameter values are such that D and T are switched around but the attractor is destroyed in the same way.

Fig. 16 shows the results of numerical simulations applied to two slices of $\boldsymbol{\Phi}^{(4)}$. The white areas just to the left of $\phi^+(\xi) = 0$ and $\phi^-(\xi) = 0$ correspond to the phenomenon that we have just described. These areas are bounded on the left by a curve of heteroclinic bifurcations. Since we cannot identify this curve with hand calculations, it is natural to attempt to compute the curve numerically with numerical continuation methods. However, we do not show the result of such a computation because we suspect this curve highly irregular, e.g. non-differentiable at infinitely many points, as explained by Osinga [28].

In each plot in Fig. 16 the attractor does in fact persist up to where the boundaries $\phi^+(\xi) = 0$ and $\phi^-(\xi) = 0$ meet. This is because on the curve $\lambda_L^s = \lambda_R^s$ the right-most point of the attractor is D and T, which are equal. Also near the top of Fig. 16-a the attractor persists slightly beyond $\phi^+(\xi) = 0$ because here the attractor fails to approach D so is not destroyed when $D = C$ at $\phi^+(\xi) = 0$.

Despite the extra complexities in $\boldsymbol{\Phi}^{(4)}$ it still appears that renormalisation is helpful for explaining the bifurcation structure. Let

$$\mathcal{R}_0^{(4)} = \left\{ \xi \in \boldsymbol{\Phi}^{(4)} \,\middle|\, \phi_{\min}(\xi) > 0,\ \phi_{\min}(g(\xi)) \le 0,\ \alpha(\xi) < 0 \right\}. \tag{39}$$

Based on Fig. 16 we conjecture that for any $\xi \in \mathcal{R}_0^{(4)}$, if (1) has an attractor then this attractor is chaotic with one connected component. Now let

$$\mathcal{R}_n^{(4)} = \left\{ \xi \in \boldsymbol{\Phi}^{(4)} \,\middle|\, \phi_{\min}(g^n(\xi)) > 0,\ \phi_{\min}(g^{n+1}(\xi)) \le 0,\ \alpha(\xi) < 0, \alpha(g(\xi)) < 0 \right\}. \tag{40}$$

Unlike in previous sections here we have included the extra constraint $\alpha(g(\xi)) < 0$ so that the $\mathcal{R}_n^{(4)}$ do not include the region $\mathcal{P}_4$, defined to be where (1) has a stable period-four solution with symbolic itinerary $LRRR$. This region is visible in Fig. 16-b and shown more clearly in the magnification, Fig. 17. Note that here we do not show the result of the numerics because the component counting algorithm does not work efficiently close to the curve $\alpha(g(\xi)) = 0$. The following result is a trivial consequence of our definitions.

Proposition 9.1. *If $\xi \in \mathcal{R}_n^{(4)}$ with $n \ge 1$, then $g(\xi) \in \mathcal{R}_{n-1}^{(3)}$.*

Based on this we conjecture that for any $\xi \in \mathcal{R}_n^{(4)}$ with $n \ge 1$ the map (1) has a chaotic attractor with exactly 2^n connected components, and this is supported by the numerics in Fig. 16. Fig. 18-a shows the attractor of (1) for a typical parameter point in $\mathcal{R}_1^{(4)}$, specifically

$$\xi_{\text{ex}}^{(4)} = (2.2, -0.4, -1.5, 0.4). \tag{41}$$

As expected it has two connected components, one of which is contained in Π_ξ, and both of which are affine transformations of the single-component attractor of (1.1) with $g\left(\xi_{\text{ex}}^{(4)}\right) \in \mathcal{R}_0^{(3)}$ shown in Fig. 18-b.

10. Reduction to one dimension

Finally we address a novelty of the non-invertible settings. In these settings the stable eigenvalues λ_L^s and λ_R^s have the same sign (they are both positive if $\delta_L > 0$ and $\delta_R < 0$, and both negative if $\delta_L < 0$ and $\delta_R > 0$), so it is possible for them to be equal. From

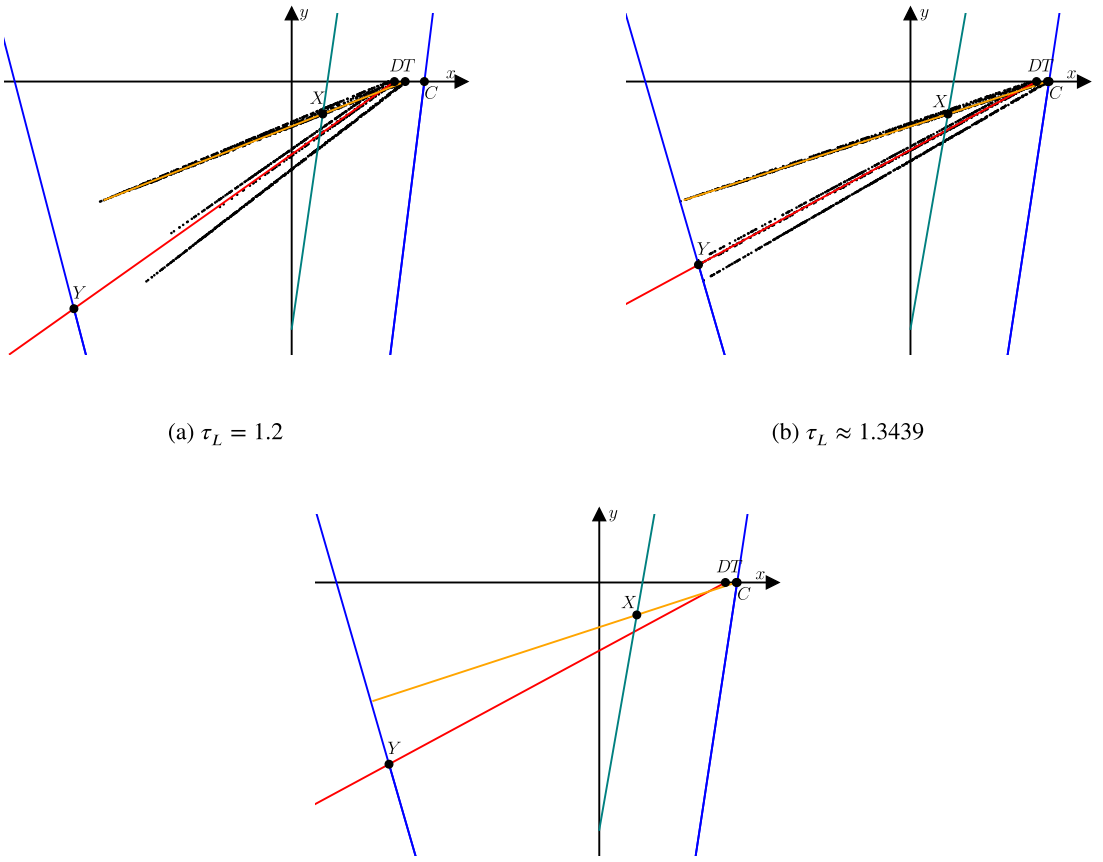

(a) $\tau_L = 1.2$ (b) $\tau_L \approx 1.3439$

(c) $\tau_L = 1.35$

Fig. 14. Phase portraits of (1) with $\delta_L = -0.4$, $\delta_R = 0.4$, $\tau_R = -2.8$, and three different values of τ_L corresponding to the blue triangles in Fig. 16-a. The parameter value used in panel (b) is approximately where the attractor is destroyed. In all three panels D lies to the left of T which lies to the left of C.

the formulas (11) and (12) for the points D and T we have

$$D_1 - T_1 = \frac{\lambda_L^s - \lambda_R^s}{\left(1-\lambda_L^s\right)\left(1-\lambda_R^s\right)}. \tag{42}$$

Thus D and T coincide when the stable eigenvalues are equal. Thus the boundaries $\phi^+(\xi) = 0$ and $\phi^-(\xi) = 0$, where $C = D$ and $C = T$ respectively, intersect where $\lambda_L^s = \lambda_R^s$, and this is evident in Figs. 12 and 16. Also for each $n \geq 1$ the boundaries $\phi^+(g^n(\xi)) = 0$ and $\phi^-(g^n(\xi)) = 0$ intersect where $\lambda_L^s = \lambda_R^s$.

We now show that if $\lambda_L^s = \lambda_R^s$ then the pertinent dynamics reduces to one dimension, as in Fig. 19.

Proposition 10.1. *If $\xi \in \Phi$ with $\phi_{\min}(\xi) > 0$ and $\lambda_L^s = \lambda_R^s$, then f_ξ is forward invariant on the line segment from T to $f_\xi(T)$. Moreover, on this segment f_ξ is conjugate to the skew tent map*

$$z \mapsto \begin{cases} \lambda_L^u z + 1, & z \leq 0, \\ \lambda_R^u z + 1, & z \geq 0, \end{cases} \tag{43}$$

on $\left[\lambda_R^u + 1, 1\right]$.

Proof. The line segment from T to $f_\xi(T)$ is

$$\Gamma = \left\{ \gamma(z) \,\middle|\, z \in \left[\lambda_R^u + 1, 1\right] \right\}, \text{ where } \gamma(z) = \left(\frac{z}{1-\lambda_R^s}, \frac{(1-z)\lambda_R^s}{1-\lambda_R^s} \right),$$

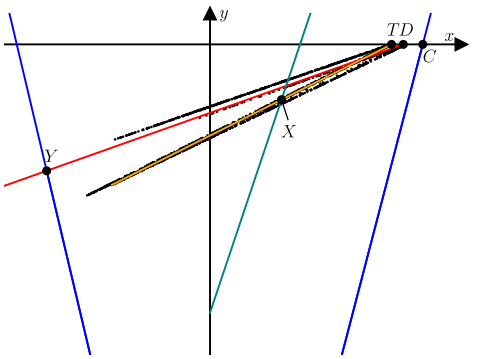

(a) $\tau_L = 2$

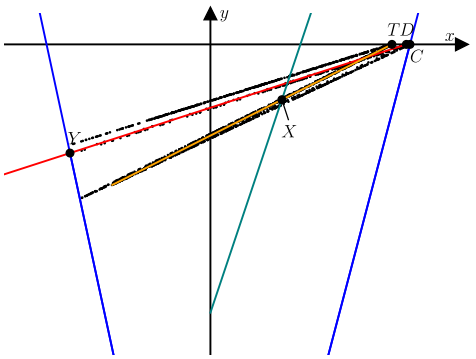

(b) $\tau_L \approx 2.2285$

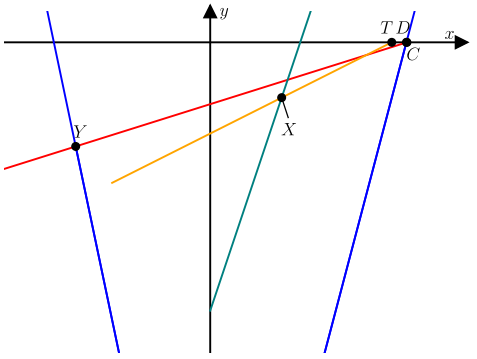

(c) $\tau_L = 2.3$

Fig. 15. Phase portraits of (1) with $\delta_L = -0.4$, $\delta_R = 0.4$, $\tau_R = -1.8$, and three different values of τ_L corresponding to the black triangles in Fig. 16-a. The parameter value used in panel (b) is approximately where the attractor is destroyed. In all three panels T lies to the left of D which lies to the left of C.

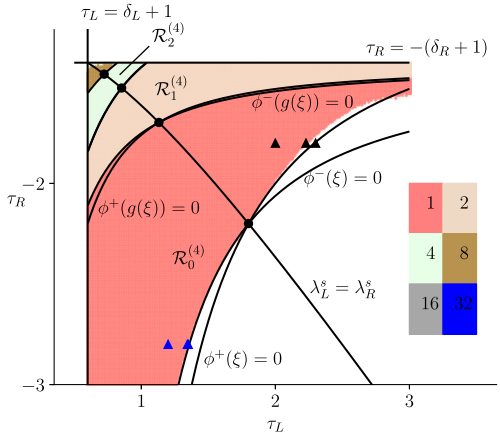

(a) $\delta_L = -0.4, \delta_R = 0.4$.

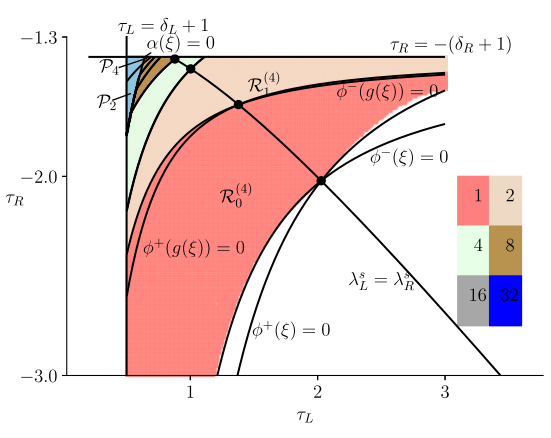

(b) $\delta_L = -0.5, \delta_R = 0.4$.

Fig. 16. Two-dimensional slices of the non-invertible parameter region $\Phi^{(4)}$ showing the bifurcation curves overlaid upon numerical results obtained using $\epsilon = 0.001$ and $M = 10^6$. The blue [black] triangles correspond to the parameter values of Fig. 14 [Fig. 15].

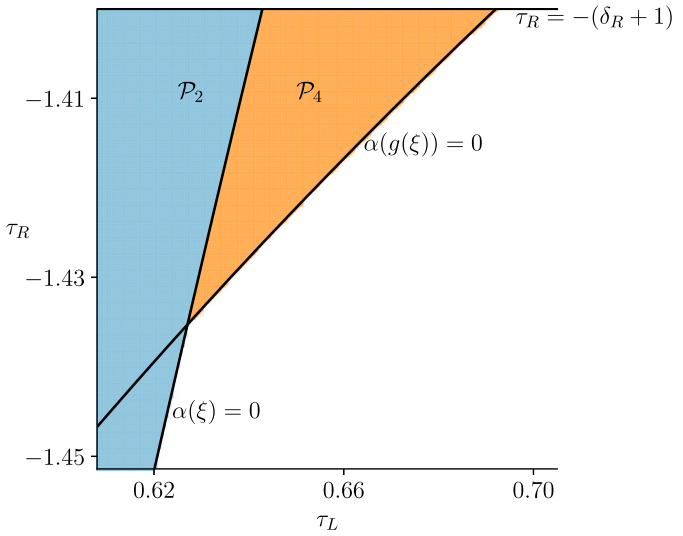

Fig. 17. A magnified version of Fig. 16-b showing the regions having a stable LR-cycle (period-two solution) and a stable $LRRR$-cycle (period-four solution).

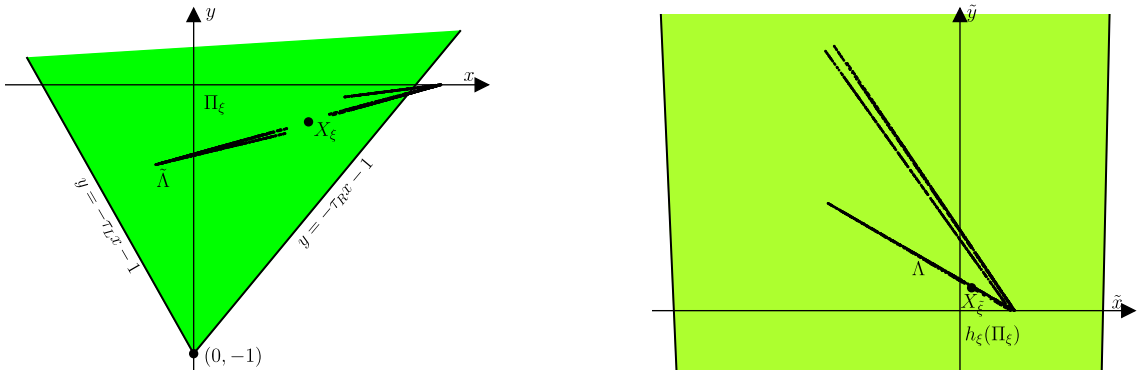

(a) $\xi = \xi_{\text{ex}}^{(4)} \in \mathcal{R}_1^{(4)}$ (b) $\xi = g\left(\xi_{\text{ex}}^{(4)}\right) \in \mathcal{R}_0^{(3)}$

Fig. 18. Panel (a) is a phase portrait of (1) at the parameter point $\xi_{\text{ex}}^{(4)}$ (41) where the attractor has two connected components in the $\delta_L < 0$ non-invertible case. Panel (b) uses instead $g\left(\xi_{\text{ex}}^{(4)}\right)$.

because putting $z = 1$ gives $(x, y) = \left(\frac{1}{1-\lambda_R^s}, 0\right) = T$ by (11), while putting $z = \lambda_R^u + 1$ gives $(x, y) = \left(\frac{1+\lambda_R^u}{1-\lambda_R^s}, \frac{-\lambda_R^s \lambda_R^u}{1-\lambda_R^s}\right)$ which is identical to $f_\xi(T) = (\tau_R T_1 + 1, -\delta_R T_1)$ (since $\tau_R = \lambda_R^s + \lambda_R^u$ and $\delta_R = \lambda_R^s \lambda_R^u$). If $z \in [0, 1]$ then

$$f_\xi(\gamma(z)) = \left(\tau_R x + y + 1, -\delta_R x\right) = \left(\frac{1 + \lambda_R^u z}{1 - \lambda_R^s}, \frac{-\lambda_R^s \lambda_R^u z}{1 - \lambda_R^s}\right) = \gamma(\lambda_R^u z + 1),$$

while if $z \in [\lambda_R^u + 1, 1]$ then

$$f_\xi(\gamma(z)) = \left(\tau_L x + y + 1, -\delta_L x\right) = \left(\frac{1 + \lambda_L^u z}{1 - \lambda_R^s}, \frac{-\lambda_R^s \lambda_L^u z}{1 - \lambda_R^s}\right) = \gamma(\lambda_L^u z + 1),$$

and the result follows. □

Notice $\lambda_L^u > 1$ and $\lambda_R^u < -1$, which corresponds in Fig. 2 to a point in some $\mathcal{R}_n$, with $n \geq 0$. Thus, with this value of n, the attractor of the skew tent map (43) is comprised of 2^n disjoint intervals. Consequently the attractor of f_ξ is comprised of 2^n disjoint line segments. Places where the value of n changes can be computed by solving for where $\phi_0 \circ g^n = 0$ in Fig. 2. We computed these points numerically and have plotted them as black dots in Figs. 12 and 16 from which we see that, as expected, these points are where $\phi^+ \circ g^n = 0$ and $\phi^- \circ g^n = 0$. In this way the conjectures in Sections 8 and 9 on the number of connected components of the attractors are confirmed in the special codimension-one scenario that the stable stability multipliers associated with X and Y are equal.

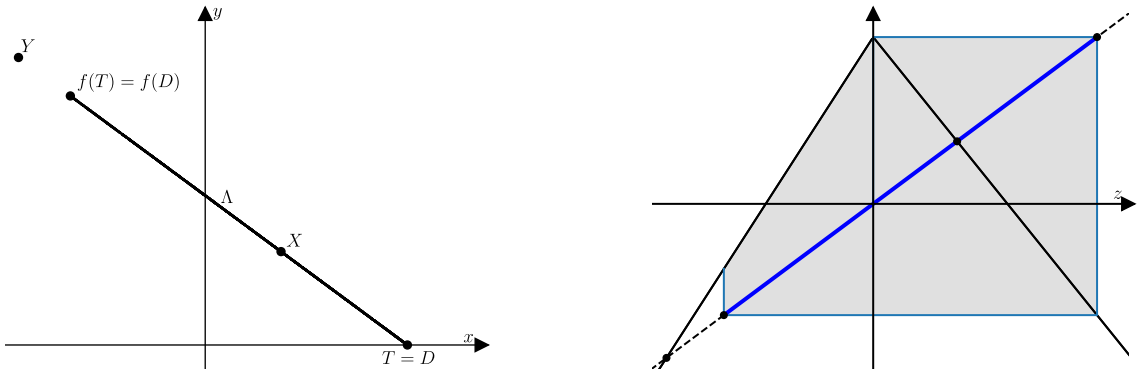

(a) $\xi = (2.323, 0.5, -1.427, -0.4)$ (b) corresponding cobweb diagram

Fig. 19. Panel (a) shows the attractor of (1) at the given parameter point which belongs to $\mathcal{R}_0^{(3)}$. This attractor is the line segment from T to $f_\xi(T)$. The restriction of f_ξ to the attractor is the one-dimensional map (43) indicated in panel (b).

11. Discussion

It has long been known that symmetric tent maps and skew tent maps readily admit attractors with 2^n connected components, and that for any given slopes for the two pieces of the map the value of n can be determined through renormalisation. Here we have shown how this can be realised for two-dimensional maps and uncovered some novel complexities relating to the possibility of stable period-two and period-four solutions. We have also shown how the attractor can be destroyed at heteroclinic bifurcations (boundary crises) that cannot be characterised algebraically.

It remains to verify the conjectures in Sections 7–9 on the number of connected components of the attractor in the various parameter regions we have defined. We feel this should be possible by following the methodology used in [13] but suspect it will be a substantial undertaking. Chaos in higher-dimensional piecewise-linear maps has applications to cryptography [19], and it remains to see what aspects of the renormalisation can be described for the N-dimensional border-collision normal form [36] with no restriction on N. Also it remains to see if renormalisation schemes based on other symbolic substitution rules can be used to explain parameter regimes where (1) has attractors with other numbers of components, e.g. three components, as described in [14].

Finally we note that Proposition 10.1 provides a rare example of dimension reduction in a piecewise-smooth setting. Dimension reduction is core element of smooth bifurcation theory whereby centre manifolds allow us to explain the dynamics of high dimensional systems with low dimensional equations [20]. In general the bifurcation theory of piecewise-smooth systems is hampered by an inability to do this usually centre manifolds do not exist [5]. It remains to see how far Proposition 10.1 can be generalised to help us understand border-collision bifurcations involving two eigenvalues that are identical, or are nearly identical.

CRediT authorship contribution statement

Indranil Ghosh: Conceptualization, Formal analysis, Investigation, Methodology, Project administration, Resources, Software, Validation, Visualization, Writing – original draft, Writing – review & editing. **Robert I. McLachlan:** Conceptualization, Supervision, Writing – review & editing. **David J.W. Simpson:** Conceptualization, Funding acquisition, Investigation, Methodology, Supervision, Validation, Writing – review & editing.

Declaration of competing interest

The authors declare that they have no known competing financial interests or personal relationships that could have appeared to influence the work reported in this paper.

Data availability

The data that support the findings of this study are available within the article.

Acknowledgements

This work was supported by Marsden Fund contracts MAU1809 and MAU2209 managed by Royal Society Te Apārangi.

References

[1] Avrutin V, Eckstein B, Schanz M. On detection of multi-band chaotic attractors. Proc R Soc Lond Ser A Math Phys Eng Sci 2007;463(2081):1339–58.
[2] Banerjee S, Grebogi C. Border collision bifurcations in two-dimensional piecewise smooth maps. Phys Rev E 1999;59(4):4052.
[3] Banerjee S, Verghese G, editors. Nonlinear phenomena in power electronics. New York: IEEE Press; 2001.
[4] Banerjee S, Yorke J, Grebogi C. Robust chaos. Phys Rev Lett 1998;80(14):3049–52.
[5] di Bernardo M, Budd C, Champneys A, Kowalczyk P. Piecewise-smooth dynamical systems: theory and applications. Vol. 163, New York: Springer-Verlag; 2008.
[6] di Bernardo M, Tse C. Chaos in power electronics: An overview. Chaos Circuits Syst 2002;317–40.
[7] Burns R. Advanced control engineering. Oxford: Butterworth-Heinemann; 2001.
[8] Buzzi J. Absolutely continuous invariant measures for generic multi-dimensional piecewise affine expanding maps. Int J Bifurcation Chaos 1999;9(9):1743–50.
[9] Eckstein B. Bandcounter: counting bands of multiband chaotic attractors. Universitätsbibliothek der Universität Stuttgart; 2006.
[10] Fatoyinbo H, Simpson D. A synopsis of the non-invertible, two-dimensional, border-collision normal form with applications to power converters. Int J Bifurcation Chaos 2023;33(8):2330019.
[11] Ghosh I, McLachlan R, Simpson D. Robust chaos in orientation-reversing and non-invertible two-dimensional piecewise-linear maps. 2023, arXiv preprint arXiv:2307.05144.
[12] Ghosh I, Simpson D. Robust devaney chaos in the two-dimensional border-collision normal form. Chaos 2022;32(4):043120.
[13] Ghosh I, Simpson DJW. Renormalization of the two-dimensional border-collision normal form. Int J Bifurcation Chaos 2022;32(12):2250181.
[14] Glendinning PA, Simpson DJW. Robust chaos and the continuity of attractors. Trans Math Appl 2020;4(1):tnaa002.
[15] Haydn N, Lacroix Y, Vaienti S. Hitting and return times in ergodic dynamical systems. Ann Probab 2005;33(5):2043–50.
[16] Ibarz B, Casado J, Sanjuán M. Map-based models in neuronal dynamics. Phys Rep 2011;501:1–74.
[17] Ito S, Tanaka S, Nakada H. On unimodal linear transformations and chaos. Proc Japan Acad 1979;55(Ser. A):231–6.
[18] Ito S, Tanaka S, Nakada H. On unimodal linear transformations and chaos II. Tokyo J Math 1979;2(2):241–59.
[19] Kocarev L, Lian S, editors. Chaos-based cryptography: theory, algorithms and applications. New York: Springer; 2011.
[20] Kuznetsov Y. Elements of applied bifurcation theory, vol. 112, Springer; 2004.
[21] Lasota A, Yorke J. On the existence of invariant measures for piecewise monotonic transformations. Trans Amer Math Soc 1973;186:481–8.
[22] Li T, Yorke J. Ergodic transformations from an interval into itself. Trans Amer Math Soc 1978;235(1):183–92.
[23] Liberzon D. Switching in systems and control. Boston: Birkhauser; 2003.
[24] Maistrenko Y, Maistrenko V, Chua L. Cycles of chaotic intervals in a time-delayed Chua's circuit. Int J Bifur Chaos 1993;3(6):1557–72.
[25] Misiurewicz M. Strange attractors for the lozi mappings. Nonlinear Dyn Ann NY Acad Sci 1980;357(1):348–58.
[26] Nusse H, Yorke J. Border-collision bifurcations including "period two to period three" for piecewise smooth systems. Phys D 1992;57(1–2):39–57.
[27] Nusse H, Yorke J. Border-collision bifurcations for piecewise-smooth one-dimensional maps. Int J Bifur Chaos 1995;5(1):189–207.
[28] Osinga HM. Boundary crisis bifurcation in two parameters. J Differ Equ Appl 2006;12(10):997–1008.
[29] Ou D. Critical points in higher dimensions, I: Reverse order of periodic orbit creations in the Lozi family. 2022, arXiv preprint arXiv:2203.02326.
[30] Pesin Y. Dynamical systems with generalized hyperbolic attractors: hyperbolic, ergodic and topological properties. Ergod Theory Dyn Syst 1992;12:123–51.
[31] Pumariño A, Rodríguez JÁ, Vigil E. Renormalization of two-dimensional piecewise linear maps: Abundance of 2-D strange attractors. Discrete Contin Dyn Syst 2018;38:941–66.
[32] Pumariño A, Rodríguez JÁ, Vigil E. Persistent two-dimensional strange attractors for a two-parameter family of expanding baker maps. Discrete Contin Dyn Syst Ser B 2019;24(2):657–70.
[33] Puu T, Sushko I. Business cycle dynamics: models and tools. New York: Springer-Verlag; 2006.
[34] Robins V, Meiss J, Bradley E. Computing connectedness: Disconnectedness and discreteness. Physica D 2000;139(3–4):276–300.
[35] Rychlik M. Invariant measures and the variational principle for lozi mappings. In: The theory of chaotic attractors. New York: Springer; 2004, p. 190–221.
[36] Simpson D. Border-collision bifurcations in $\mathbb{R}^n$. SIAM Rev 2016;58(2):177–226.
[37] Simpson D. Unfolding homoclinic connections formed by corner intersections in piecewise-smooth maps. Chaos 2016;26(7):073105.
[38] Simpson D, Meiss J. Neimark-sacker bifurcations in planar, piecewise-smooth, continuous maps. SIAM J Appl Dyn Syst 2008;7(3):795–824.
[39] Sushko I, Avrutin V, Gardini L. Bifurcation structure in the skew tent map and its application as a border collision normal form. J Differ Equ Appl 2016;22(8):1040–87.
[40] Sushko I, Gardini L. Center bifurcation for two-dimensional border-collision normal form. Int J Bifurcation Chaos 2008;18(4):1029–50.
[41] Szalai R, Osinga H. Arnol'd tongues arising from a grazing-sliding bifurcation. SIAM J Appl Dyn Syst 2009;8(4):1434–61.
[42] Tsujii M. Absolutely continuous invariant measures for expanding piecewise linear maps. Invent Math 2001;143:349–73.
[43] Tsypkin Y. Relay control systems. New York: Cambridge University Press; 1984.
[44] Veitch D, Glendinning P. Explicit renormalisation in piecewise linear bimodal maps. Physica D 1990;44(1–2):149–67.
[45] Young L-S. Bowen–Ruelle measures for certain piecewise hyperbolic maps. Trans Amer Math Soc 1985;287(1):41–8.
[46] Zhusubaliyev Z, Mosekilde E. Bifurcations and chaos in piecewise-smooth dynamical systems. World Scientific, Singapore; 2003.
[47] Zhusubaliyev Z, Mosekilde E, Maity S, Mohanan S, Banerjee S. Border collision route to quasiperiodicity: Numerical investigation and experimental confirmation. Chaos 2006;16(2):023122.